

Continuous variable quantum computation of the $O(3)$ model in $1 + 1$ dimensions

Raghav G. Jha,^a Felix Ringer,^{a,b} George Siopsis,^c Shane Thompson^c

^a*Thomas Jefferson National Accelerator Facility, Newport News, VA 23606, USA*

^b*Department of Physics, Old Dominion University, Norfolk, VA 23529, USA*

^c*Department of Physics and Astronomy, University of Tennessee, Knoxville, Tennessee 37996-1200, USA*

E-mail: raghav.govind.jha@gmail.com, fmringer@jlab.org,
siopsis@tennessee.edu, sthomp78@vols.utk.edu

ABSTRACT: We formulate the $O(3)$ non-linear sigma model in $1 + 1$ dimensions as a limit of a three-component scalar field theory restricted to the unit sphere in the large squeezing limit. This allows us to describe the model in terms of the continuous variable (CV) approach to quantum computing. We construct the ground state and excited states using the coupled cluster ansatz and find excellent agreement with the exact diagonalization results for a small number of lattice sites. We then present the simulation protocol for the time evolution of the model using CV gates, estimate the discretization error, and present numerical results obtained from a photonic quantum simulator. We expect that the methods developed in this work will be useful for exploring interesting dynamics for a wide class of sigma models and gauge theories, as well as for simulating scattering events on quantum hardware in the coming decade.

Contents

1	Introduction	1
2	Description of the the $O(3)$ sigma model - a toy model for QCD	2
3	Scalar field theory formulation on the unit sphere	7
4	Quantum simulation using continuous variables	13
4.1	Coupled Cluster Ansatz	13
4.2	Quantum computation of energy levels	17
4.3	Time evolution circuits and quantum simulator results	21
5	Conclusion	23
A	Continuous Variable Gates	25
A.1	Single qumode gates	25
A.2	Two qumode gates	27

1 Introduction

All the fundamental interactions in nature except gravity have been successfully described within the framework of quantum field theory. A proper understanding of the dynamics of the real-time dynamics of these interacting field theories is still an open problem in higher dimensions. In lower dimensions, some progress has been achieved using classical computations based on MPS/PEPS tensor network methods. However, for theories close to the critical point these methods cannot be reliable tools because these methods can only represent ground states of a special class of local Hamiltonians with gapped spectrum due to its low entanglement. Another limitation is that even for systems with a gapped spectrum, the growth of entanglement during the time of evolution can sometimes render these methods ineffective. This limitation using classical methods is well-suited for quantum computers. This has led to continued efforts in understanding various toy models using quantum computation methods. Due to the current limitations on hardware resources, it is not possible to study the real-time dynamics of QCD in four dimensions. This leads one to consider simpler toy models with lower dimensions. In this regard, the $O(3)$ sigma model in 1+1 dimensions is a particularly interesting playground. This model shares some interesting properties with QCD, the most important of which is the ‘asymptotic freedom’ [1]. It has a dynamical mass gap and also admits instantons similar to the four-dimensional QCD [2]. This makes it a preferred toy model [3] to explore fundamental questions. Though this model has been extensively studied numerically, this has recently again attracted a lot of attention because

new classical and quantum computing methods have been developed and this model is again relevant as a toy model. This model has been studied using tensor network methods based on matrix product states (MPS) for $\theta = 0, \pi$ [4, 5] and using higher-order tensor renormalization group methods [6]. We are here concerned with aspects of quantum computation. In order to regularize the theory and carry out numerical computations, past works have mostly focused on using qubit approach to quantum computing [7–9]. The qubitization program has argued that to reproduce the critical point of the continuum field theory in this model, only two qubits per site are required. In this work, we present an alternate method that is a more natural setting for bosonic degrees of freedom such as the $O(3)$ model. This approach is known as continuous variable (CV) quantum computation [10] and is an alternative to the more traditional qubit methods. The fundamental idea of the CV approach is to not consider a system of two-state systems such as ‘qubits’ or d -state systems such as ‘qudits’ but to harness the power of the infinite-dimensional representation in terms of bosonic fields obeying the infinite-dimensional commutator relations. In addition to the access to the enhanced Hilbert space, a quantum computer based on the CV approach can effectively make use of photonic elements [11] to build states that are better suited for maintaining coherence and quantum error correction.

The outline of the paper is as follows. In Sec. 2, we describe the standard rotor Hamiltonian which describes the lattice version of the sigma model in one spatial dimension. We then present the qumode formulation in Sec. 3. Then in Sec. 4.1, we consider the coupled cluster Ansatz for the ground state of the $O(3)$ model. We present the protocol to measure energy expectation value and do time evolution of the model in Sec. 4. We end the paper with a summary and conclusion in Sec. 5. We provide additional details about the CV gates in Appendix A.

(FR: Some more recent references we should briefly comment on in the introduction [12–14]. Strawberry fields reference [15]. Examples of recent progress in photonic quantum computing [16–18]. Will add text later, just put all Refs. here for now.)

I agree. We should add these additional references

Alt possibility

2 Description of the the $O(3)$ sigma model - a toy model for QCD

Nonlinear sigma models have been extensively studied because they share several features with gauge theories but without added complications related to maintaining gauge invariance. An important application of these models is in the low-energy dynamics of pions described by an effective chiral Lagrangian density given schematically by $\mathcal{L} = \frac{1}{4} \text{Tr}[\partial_\mu U \partial^\mu U^\dagger]$, where U is an isospin $SU(2)$ matrix. Due to this reason, this is also sometimes referred to as a “principal chiral field” model [19]. It has a global $SU(2)_L \times SU(2)_R$ symmetry which coincides with the $O(4)$ symmetry of the sigma model. This is clearly seen if we parametrize the isospin matrix as $U = n_0 + i\mathbf{n} \cdot \boldsymbol{\sigma}$, where $\boldsymbol{\sigma} = (\sigma_1, \sigma_2, \sigma_3)$ are Pauli matrices, and $n_a n^a \equiv n_0^2 + \mathbf{n}^2 = 1$. We can define the angular momenta as $J_{ab} = -i(n_a \frac{\partial}{\partial n_b} - n_b \frac{\partial}{\partial n_a})$ with

$a, b = 0, 1, 2, 3$. The Hamiltonian discretized on a spatial lattice can be written as

$$H = \frac{1}{2\lambda} \sum_{a,b} J_{ab}^2 - \lambda \sum_{\langle x, x' \rangle} n_a(x) n^a(x') \quad (2.1)$$

where λ is a coupling constant. The potential is bi-linear in the vectors n_a that act as coordinates of the system.

Moreover, a gauge theory with a local $SU(2)$ symmetry can also be formulated in terms of the parametrized isospin matrix on the lattice. In this case, the matrices U reside on the links along which one also defines angular momenta J_{ab} . The Hamiltonian can be written as

$$H = \frac{1}{2\lambda} \sum_{\text{links}} J_{ab}^2 - \frac{\lambda}{2} \sum_{\text{plaquettes}} \text{Tr}[U(1)U(2)U(3)U(4)] \quad (2.2)$$

where we introduced the Wilson loop over a plaquette in the second term. It can be expressed in terms of the four-dimensional vectors $n_a(i)$ with $i = 1, 2, 3, 4$. We obtain a quadri-linear expression for the plaquette term

$$\begin{aligned} \frac{1}{2} \text{Tr}[U(1)U(2)U(3)U(4)] &= n^a(1)n_a(2) n^b(3)n_b(4) - n^a(1)n_a(3) n^b(2)n_b(4) \\ &\quad + n^a(1)n_a(4) n^b(2)n_b(3) + \epsilon^{abcd} n_a(1)n_b(2)n_c(3)n_d(4). \end{aligned} \quad (2.3)$$

The states obey the constraint $\epsilon^{abcd} J_{ab} J_{cd} |\Psi\rangle = 0$. Additionally, the system also obeys Gauss's Law which further constrains the Hilbert space to the gauge singlet sector [20]. However, in this work, we will focus on quantum computations using continuous variables for a simpler system, the nonlinear $O(3)$ sigma model, which shares important features with theories relevant to understanding strong interactions but is easier to tackle. We leave extensions of the approach taken in this paper to formulate the continuous variable formulation of gauge theories for future works. The nearest-neighbor $O(3)$ sigma model Hamiltonian is given by [21]

$$H = \frac{1}{2g^2} \sum_i \mathbf{L}_i^2 - g^2 \sum_{\langle i, j \rangle} \mathbf{n}_i \cdot \mathbf{n}_j. \quad (2.4)$$

Here g^2 is the coupling constant, i and j index nearest neighbor sites on a uni-directional lattice. In addition, \mathbf{n}_i is a unit 3-vector at site i , which takes values on \mathbb{S}_2 and \mathbf{L}_i is the angular momentum operator at each site $L^a = \frac{1}{2} \epsilon^{abc} J_{bc}$. We use periodic boundary conditions. As is customary, we write the interaction term in terms of spherical coordinates noting that the vectors \mathbf{n}_i have unit modulus:

$$\mathbf{n}_i \cdot \mathbf{n}_j = \sin \theta_i \sin \theta_j \cos(\phi_i - \phi_j) + \cos \theta_i \cos \theta_j. \quad (2.5)$$

In fact, one can express the dot product of the vectors in terms of spherical harmonics $Y_{l,m}(\theta, \phi)$ as:

$$\mathbf{n}_i \cdot \mathbf{n}_j = \frac{4\pi}{3} \left(Y_{1,0}(\theta_i, \phi_i) Y_{1,0}(\theta_j, \phi_j) - Y_{1,1}(\theta_i, \phi_i) Y_{1,-1}(\theta_j, \phi_j) - Y_{1,-1}(\theta_i, \phi_i) Y_{1,1}(\theta_j, \phi_j) \right). \quad (2.6)$$

Each term in (2.6) has a total magnetic quantum number equal to zero. We can also write the interaction term in terms of $n^\pm = (n^x \pm in^y)/\sqrt{2}$ as [21]

$$\mathbf{n}_i \cdot \mathbf{n}_j = n_i^+ n_j^- + n_i^- n_j^+ + n_i^z n_j^z. \quad (2.7)$$

Therefore, the lattice Hamiltonian of the 1+1-dimensional $O(3)$ model can be written as:

$$H = \frac{1}{2g^2} \sum_{x=0}^{L-1} \mathbf{L}^2(x) - g^2 \sum_{x=0}^{L-1} \left(n^+(x) n^-(x+1) + n^-(x) n^+(x+1) + n^z(x) n^z(x+1) \right), \quad (2.8)$$

and the continuum limit is obtained as we take $g^2 \rightarrow \infty$. The eigenvalues of the kinetic term is proportional to $l(l+1)$ where $l = 0 \cdots \infty$ denote the energy levels based on the irreducible representations of the $O(3)$ symmetry. However, for practical calculations, we impose a cutoff and referred to as l_{\max} . The superscripts in the components of \mathbf{n} in (2.7) have physical significance, they are proportional to $M = \pm 1, 0$ with $M = m_1 - m_2$, which correspond to different charge sectors of the $O(3)$ model. If we identify $n^\pm = \mp X_{\pm 1}$ and $n^z = X_0$, then the matrix elements of \mathbf{n} can be computed using the well-known expressions involving two Wigner-3j symbols as [22]:

$$\langle l_1, m_1 | X_M | l_2, m_2 \rangle = (-1)^{m_1} \sqrt{(2l_1+1)(2l_2+1)} \begin{pmatrix} l_1 & 1 & l_2 \\ 0 & 0 & 0 \end{pmatrix} \begin{pmatrix} l_1 & 1 & l_2 \\ -m_1 & M & m_2 \end{pmatrix}. \quad (2.9)$$

This result is obtained from the relation

$$\begin{aligned} \langle l_1, m_1 | X_M | l_2, m_2 \rangle &= \sqrt{\frac{4\pi}{3}} \int d\Omega Y_{l,m}^* Y_{1,M} Y_{l',m'} \\ &= (-1)^m \sqrt{\frac{4\pi}{3}} \int d\Omega Y_{l,-m} Y_{1,M} Y_{l',m'}, \end{aligned} \quad (2.10)$$

and the Gaunt coefficients

$$\int d\Omega Y_{l_1,m_1} Y_{l_2,m_2} Y_{l_3,m_3} = \sqrt{\frac{(2l_1+1)(2l_2+1)(2l_3+1)}{4\pi}} \begin{pmatrix} l_1 & l_2 & l_3 \\ 0 & 0 & 0 \end{pmatrix} \begin{pmatrix} l_1 & l_2 & l_3 \\ m_1 & m_2 & m_3 \end{pmatrix}. \quad (2.11)$$

In order to construct a reliable Ansatz for the $O(3)$ model, we use the coupled-cluster (CC) method which involves a state of the form [23]

$$|\psi\rangle \propto e^{\alpha \hat{T}} |\psi_0\rangle \quad (2.12)$$

where \hat{T} is the cluster operator built from single interaction terms in the Hamiltonian and α is a tunable parameter. We can include higher-interaction terms, known as doubles ansatz in the CC ansatz but for our purposes, an operator bilinear in \mathbf{n} suffices. The use of CC Ansatz for sigma models is not new and this has already been explored decades ago for a class of $O(N)$ non-linear sigma models [24–26] and recently also for quantum computations in different context [27, 28]. Depending on whether the \hat{T} is anti-Hermitian or Hermitian,

we can have a unitary or non-unitary CC trial state. To build the CC state, we start with the tensor product of the states $|l = 0, m = 0\rangle$ defined at each site

$$|\Omega_0\rangle \equiv \bigotimes_{x=0}^{L-1} |l(x) = 0, m(x) = 0\rangle, \quad (2.13)$$

which is the weak coupling vacuum state corresponding to the vanishing cluster operator $\hat{T} = 0$. We choose to express \hat{T} in terms of the potential term of the Hamiltonian and we obtain the following coupled-cluster Ansatz [29]:

$$|\text{CC}\rangle \propto \prod_x e^{\frac{2\alpha g^2}{L} \mathbf{n}(x) \cdot \mathbf{n}(x+1)} |\Omega_0\rangle, \quad (2.14)$$

where α is a variational parameter.

For $L = 2$ lattice sites, the energy of the CC state can be computed analytically. It is given by

$$\frac{E_0(\alpha)}{L} = \frac{E_0(\alpha)}{2} = -\frac{1}{4g^2} + \frac{1}{2\alpha} + \frac{\alpha - 2g^2}{2} \coth(2g^2\alpha), \quad (2.15)$$

For small g^2 , this expression is minimized for $\alpha = 0$, and we obtain the estimate of the ground state energy $E_0/2 = 0$. This corresponds to the energy of the state with zero angular momentum, as expected. Next, we observe that the optimal value of α goes to 1 for large values of g^2 . This provides the following estimate of the ground state energy

$$\frac{E_0}{2} \approx -g^2 + 1. \quad (2.16)$$

This is an expected result because at large g^2 , the potential energy dominates and it is minimized when all unit vectors $\mathbf{n}(x)$ align (since $\mathbf{n}(x) \cdot \mathbf{n}(x+1) \leq 1$).

The ground-state energy obtained using the CC state and the Hamiltonian (2.4) is shown in Figure 1. We plot $E_0(\alpha)/L$ as a function of g^2 for $L = 3$ compared to the results from exact diagonalization (ED). Using a cutoff $l_{\max} = 3$, for small g^2 , we see excellent agreement between the CC and ED results for up to $g^2 \approx 10$. For very large g^2 , the CC energies go far below the results from ED with $l_{\max} = 5$ showing that a larger cutoff is needed for accuracy of ED results.

[GS: We need to say a little more: We know that our Ansatz is accurate for large g^2 . What is a good enough l_{\max} for $g^2 = 10$? Also, for $L > 2$, we should be able to show that this Ansatz gives an accurate result for large g^2 .]

A similar approach based on a CC Ansatz which is a modified version of (2.14) can be used to estimate excited state energies. For the first excited state, we apply the CC Ansatz: (FR: Could we say a few more words where this expression is coming from?)

$$|\text{CC}_1\rangle \propto e^{\frac{2\alpha g^2}{L} \sum_x \mathbf{n}(x) \cdot \mathbf{n}(x+1)} \sum_x n_3(x) |\Omega_0\rangle \quad (2.17)$$

which is orthogonal to the CC Ansatz for the ground state $\langle \text{CC} | \text{CC}_1 \rangle = 0$. For illustration purposes, we consider again only two lattice sites $L = 2$. The Ansatz in Eq. (2.17) yields

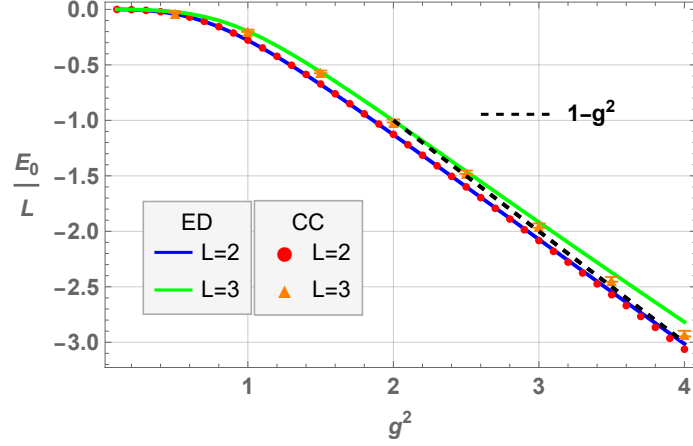


Figure 1. First pass for E_0 using ED for $L = 3$ with rotor Hamiltonian (2.4). The dashed curve is $-g^2 + 1$. The truncation level is set to $l_{\max} = 3$. [GS: Include CC result and a separate figure for $L = 2$. Do we know that $-g^2 + 1$ is the right asymptote for $L = 3$?] [No, we don't know the exact one for $L = 3$. I think one figure is enough for both $L=2$ and $L=3$ since it is sparse anyways.][ST: ED and CC for $L = 2, 3$. $l_{\max} = 3$ for ED, 500,000 sample points for MC integration for $L = 3$. $L = 2$ CC is analytic.]

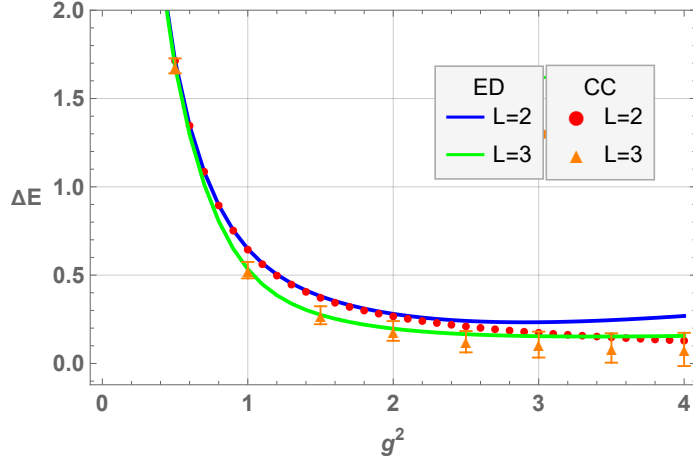


Figure 2. First pass for gap using ED with rotor Hamiltonian (2.4). [GS: Include CC result and a separate figure for $L = 2$. Same here: One figure is enough for both $L=2$ and $L=3$.][ST: ED and CC for $L = 2, 3$. $l_{\max} = 3$ for ED, 500,000 sample points for MC integration for $L = 3$. $L = 2$ CC is analytic.]

the following estimate for the energy of the first excited state

$$\frac{E_1(\alpha)}{L} = -g^2 + \frac{-\alpha + 4g^2(1 + 2g^2\alpha - \alpha^2) + e^{4g^2\alpha}(-4g^2 + \alpha + 8g^4(\alpha + \alpha^3))}{4g^2(\alpha + e^{4g^2\alpha}(-1 + 4g^2\alpha))}. \quad (2.18)$$

For small g^2 , this is minimized again for $\alpha = 0$ and we obtain the following estimate of the first excited state $\frac{E_1}{2} = \frac{1}{2g^2}$. This result corresponds to a single $l = 1$ excitation, as expected. In the large g^2 limit, the expression in Eq. (2.18) is minimized for $\alpha = 1$, similar

to the ground state, and the corresponding energy is $\frac{E_1}{2} = -g^2 + 1$. This demonstrates that the gap closes asymptotically as $g^2 \rightarrow \infty$.

First excited state energies obtained from the CC and ED methods are shown in Figure 2. As with the ground state, there is very good agreement with ED at smaller g^2 and an out-performance of the CC calculation over ED for large g^2 .

[GS: We need to say a little more: Is our Ansatz is accurate for large g^2 ? What is a good enough l_{max} for $g^2 = 10$?]

It is possible to write the $O(3)$ Hamiltonian given by (2.8) in terms of bosonic creation and annihilation operators with two quantum harmonic oscillators at each site using the Schwinger boson formalism [30]. See also Ref. [31]. Thus, it appears that only two qumodes are needed for each lattice site to simulate this model using quantum computing based on continuous variables. However, this approach results in expressions that appear to be challenging to implement with near- to intermediate-term resources.

In this work, we take an alternative point of view and express the $O(3)$ non-linear sigma model as a limit of a three-component scalar field theory in 1+1 dimensions requiring three qumodes at each site. We show that in the appropriate limit, this is equivalent to the rotor Hamiltonian which is known to reproduce the sigma model in the continuum. Both of these continuous variable approaches to the $O(3)$ model belong to the same universality class. One advantage of using the approach presented here is that scalar field theories can be simulated with established methods using continuous variable quantum computing. See Refs. [32, 33].

3 Scalar field theory formulation on the unit sphere

We now consider a linear $O(3)$ model consisting of real scalar fields $\phi^a(x)$ ($a = 1, 2, 3$) in a single spatial dimension denoted by x . We discretize space using L lattice points $x = 0, 1, \dots, L - 1$, impose periodic boundary conditions, and choose units such that the lattice spacing, and the fundamental constants c, \hbar are all set to unity. Let π^a be the conjugate momentum to ϕ^a obeying the canonical commutation relations

$$[\phi^a(x), \pi^b(x')] = i\delta^{ab}\delta_{xx'}. \quad (3.1)$$

We can write the Hamiltonian as

$$H = \frac{1}{2g^2} \sum_x \mathbf{L}^2(x) - \sum_x \left[\frac{1}{2} (\phi(x) - \phi(x+1))^2 - g^2 \right]. \quad (3.2)$$

Here the angular momentum operator \mathbf{L} denotes the cross product of the vector field and its conjugate momentum,

$$\mathbf{L}(x) = \phi(x) \times \boldsymbol{\pi}(x), \quad (3.3)$$

where we used the simplified triplet notation for the fields, $\boldsymbol{\phi} = (\phi_1, \phi_2, \phi_3)$, and similarly for $\boldsymbol{\pi}$. It is useful to define a local basis at each lattice site consisting of the states defined on a three-dimensional space

$$|l, m; \Lambda\rangle = \frac{1}{\sqrt{\mathcal{N}}} \int dr r^2 d^2\mathbf{n} e^{-\Lambda^2(r^2 - g^2)^2/8g^2} Y_{lm}(\mathbf{n}) |r, \mathbf{n}\rangle. \quad (3.4)$$

Here \mathbf{n} is a unit 3-vector, r is the radial direction, and Λ is an energy cutoff scale restricting the wavefunction on a circle of radius $r = g$. We will model the energy cutoff in terms of a squeezing parameter. The state described in (3.4) can be separated into radial and angular parts denoted by Y_{lm} . The radial integrand is not unique and any function that converges to a δ -function centered at $r = g$ as the cutoff $\Lambda \rightarrow \infty$ would work in practice. In what follows, this choice affects energies only to $\mathcal{O}(\Lambda^{-1})$. The states in (3.4) form an orthonormal set with norm

$$\mathcal{N} = \frac{g^2 \sqrt{\pi}}{\Lambda} + \mathcal{O}(\Lambda^{-3}) . \quad (3.5)$$

The matrix elements of the kinetic energy are given by exact expressions for finite values of the cutoff Λ since the radial part of the wave functions decouples

$$\frac{1}{2g^2} \langle l, m; \Lambda | \mathbf{L}^2 | l', m'; \Lambda \rangle = \frac{l(l+1)}{2g^2} \delta_{l,l'} \delta_{m,m'} . \quad (3.6)$$

For the interaction term of the Hamiltonian, we consider two adjacent sites labeled by i and j . We start with the matrix elements of a local term contributing to the interaction potential as

$$\langle l, m; \Lambda | \phi^2 | l', m'; \Lambda \rangle = g^2 (1 + \mathcal{O}(\Lambda^{-2})) \delta_{l,l'} \delta_{m,m'} . \quad (3.7)$$

The matrix elements have a simple structure and, after subtracting g^2 , see (3.2), they vanish in the limit of large values for the cutoff parameter $\Lambda \rightarrow \infty$. The matrix elements of the term involving two sites can be written as

$$\begin{aligned} & \langle l_i, m_i; \Lambda | \langle l_j, m_j; \Lambda | \phi(x_i) \cdot \phi(x_j) | l'_i, m'_i; \Lambda \rangle | l'_j, m'_j; \Lambda \rangle \\ &= g^2 (1 + \mathcal{O}(\Lambda^{-2})) \langle l_i, m_i | \langle l_j, m_j | \mathbf{n}_i \cdot \mathbf{n}_j | l'_i, m'_i \rangle | l'_j, m'_j \rangle . \end{aligned} \quad (3.8)$$

It has the same structure as the potential term of the $O(3)$ model discussed in the previous section, which we therefore recover in the limit $\Lambda \rightarrow \infty$.

Next, we use the Hamiltonian given in (3.2) with the local basis of states given in (3.4) to compute the ground state energy for different values of the cutoff Λ . The results are shown in Fig. 3, which displays the ground state energy density for $L = 2, 3$ and $l_{\max} = 3$, for three values of g^2 as a function of Λ while Figs. 4-6 display mass gaps for $L = 2$ and $L = 3$, for three values of l_{\max} and three values of Λ as function of g^2 . [GS: How do these results compare with CC results?]

To achieve a better understanding of the energy levels, we construct a variational Ansatz by extending the CC method used for the $O(3)$ model in Section 2. Analogous to (2.13), we start with a reference state $|\Omega(\Lambda)\rangle$ defined as a tensor product of the states $|l = 0, m = 0; \Lambda\rangle$ defined at each site,

$$|\Omega(\Lambda)\rangle \equiv \bigotimes_{x=0}^{L-1} |l(x) = 0, m(x) = 0; \Lambda\rangle . \quad (3.9)$$

This is the weak coupling vacuum state which corresponds to the vanishing cluster operator $\hat{T} = 0$. We define \hat{T} in terms of the potential term in the Hamiltonian and adopt the CC Ansatz:

$$|\text{CC}(\Lambda)\rangle \propto e^{-\frac{\alpha}{L} \sum_x (\phi(x) - \phi(x+1))^2} |\Omega(\Lambda)\rangle , \quad (3.10)$$

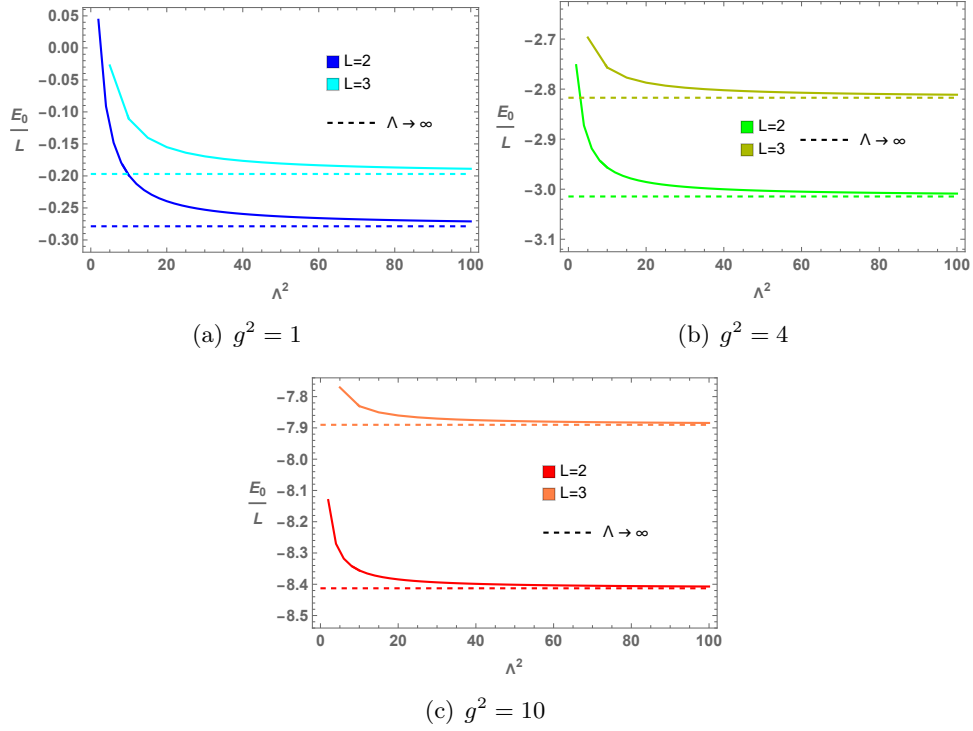


Figure 3. E_0/L vs Λ^2 for $L = 2, 3$, $l_{\max} = 3$ and three values of g^2 . Change Λ^2 to Λ .

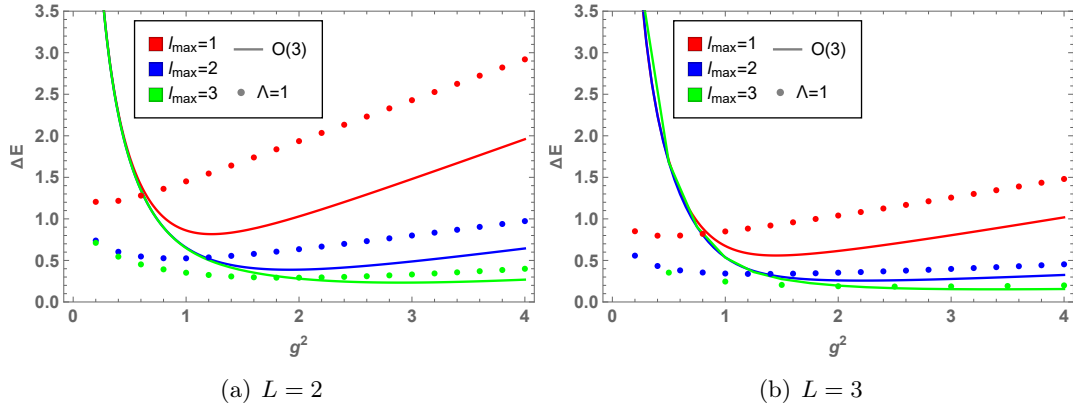


Figure 4. Mass gap ΔE vs g^2 for $L = 2, 3$, for $l_{\max} = 1, 2, 3$ and $\Lambda = 1$. Compare w/ CC

which reduces to the CC Ansatz for the $O(3)$ model (2.14) in the limit $\Lambda \rightarrow \infty$. The ground-state energy obtained using the CC state and the Hamiltonian (3.2) is shown in Figure 13, for three values of g^2 . We see excellent agreement between CC and ED results as Λ becomes large. [GS: Why are we only comparing CC with ED at infinite Λ ? In particular, we should be comparing with Figure 3. Maybe combine the two figures?]

A similar approach based on a CC Ansatz which is a modified version of (3.10) can be

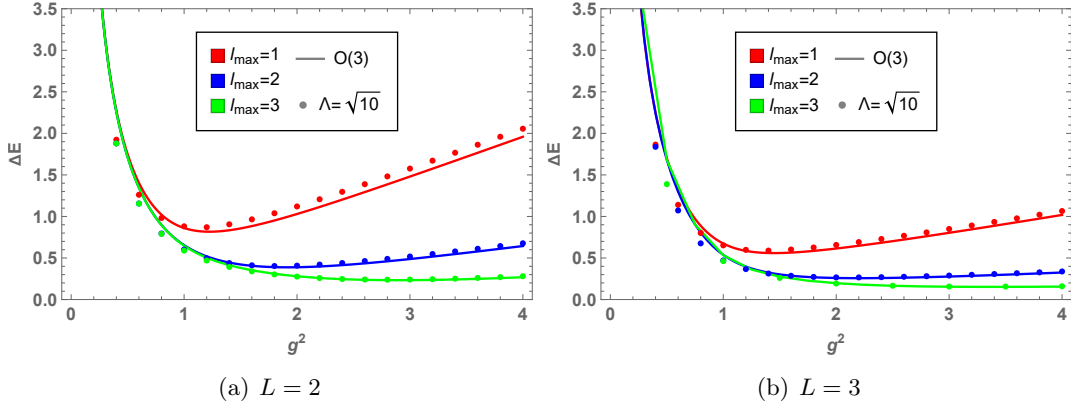


Figure 5. Mass gap ΔE vs g^2 for $L = 2, 3$, for $l_{\max} = 1, 2, 3$ and $\Lambda = \sqrt{10}$. Compare w/ CC

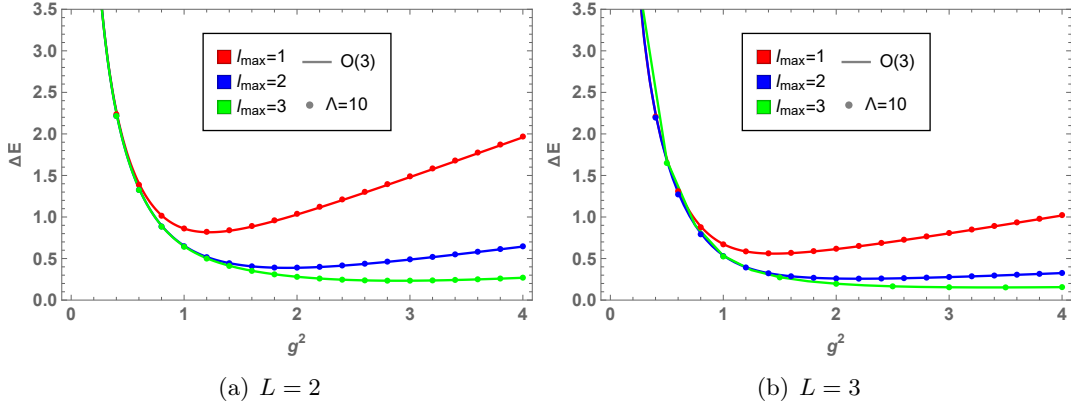


Figure 6. Mass gap ΔE vs g^2 for $L = 2, 3$, for $l_{\max} = 1, 2, 3$ and $\Lambda = 10$. Compare w/ CC

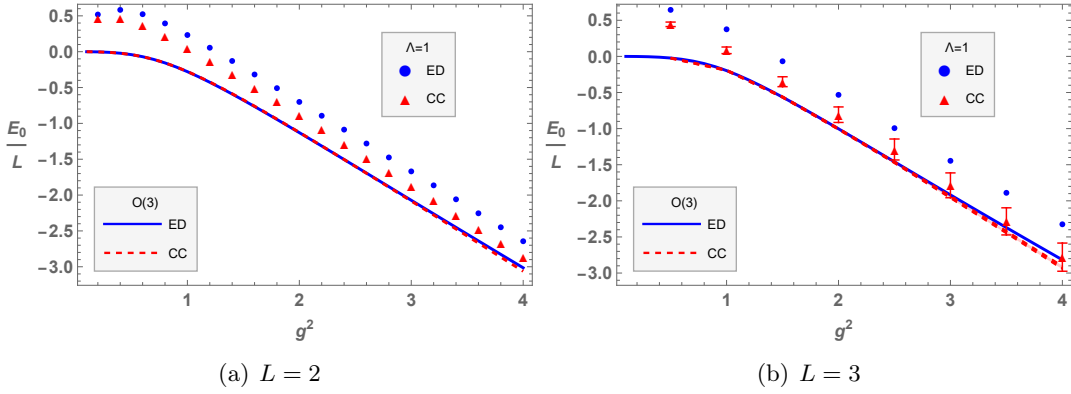


Figure 7. Ground state energy E_0/L for $L = 2, 3$ vs g^2 , computed with ED and the CC method, for $\Lambda = 1$. ED is taken at $l_{\max} = 3$.

used to estimate excited state energies. Notice that

$$|l = 1, m; \Lambda\rangle \propto Y_{1m}(\mathbf{n}) |l = 0, m = 0; \Lambda\rangle \quad (3.11)$$

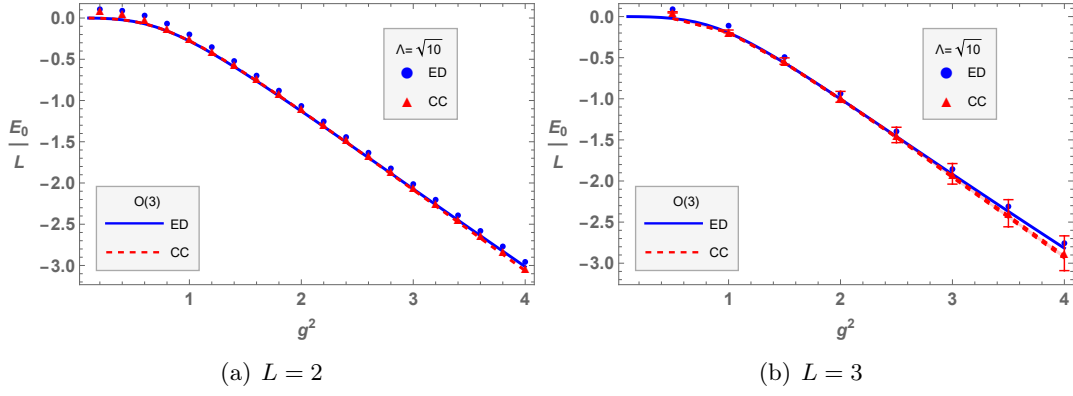


Figure 8. Ground state energy E_0/L for $L = 2, 3$ vs g^2 , computed with ED and the CC method, for $\Lambda = \sqrt{10}$. ED is taken at $l_{\max} = 3$.

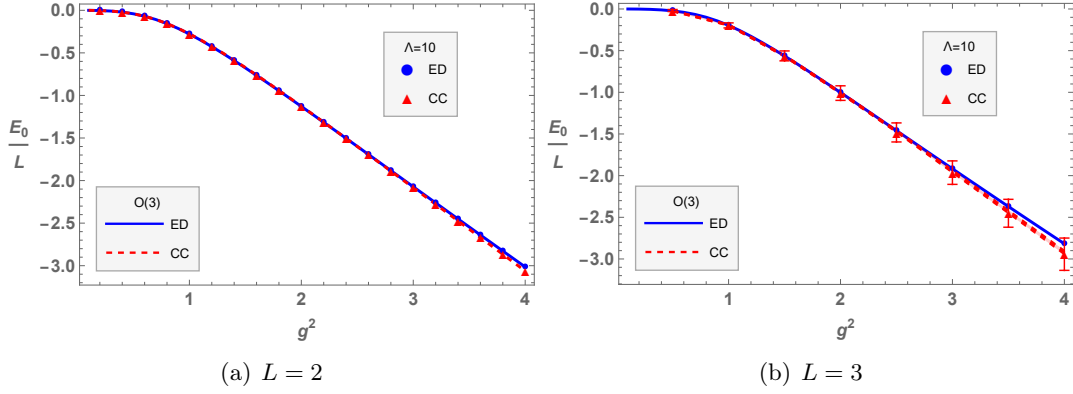


Figure 9. Ground state energy E_0/L for $L = 2, 3$ vs g^2 , computed with ED and the CC method, for $\Lambda = 10$. ED is taken at $l_{\max} = 3$.

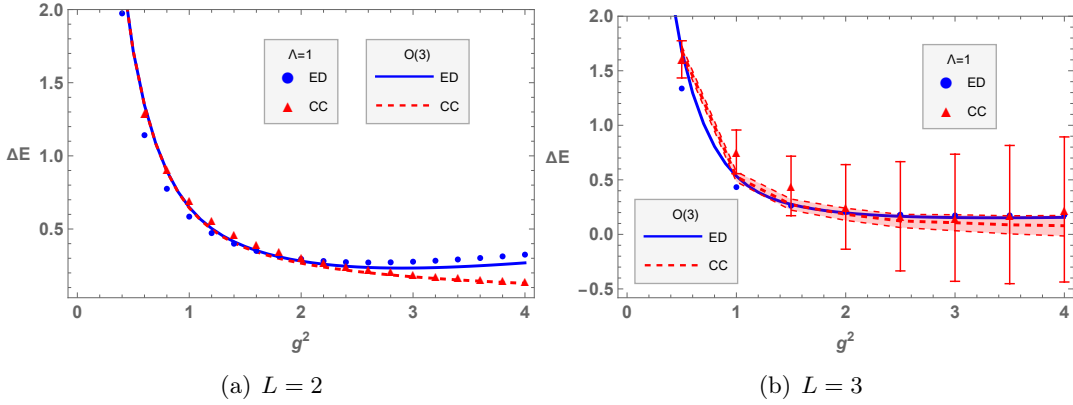


Figure 10. Mass gap ΔE for $L = 2, 3$ vs g^2 , computed with ED and the CC method, for $\Lambda = 1$. ED is taken at $l_{\max} = 3$. ED disagrees w/ green points in Fig 4

which is a direct consequence of Eq. (3.4). Concentrating on $m = 0$ (the other cases can

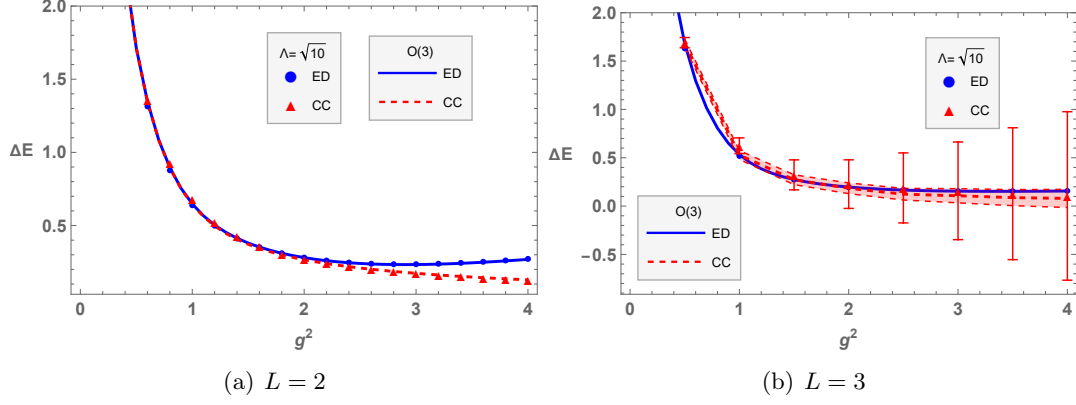


Figure 11. Mass gap ΔE for $L = 2, 3$ vs g^2 , computed with ED and the CC method, for $\Lambda = \sqrt{10}$. ED is taken at $l_{\max} = 3$.

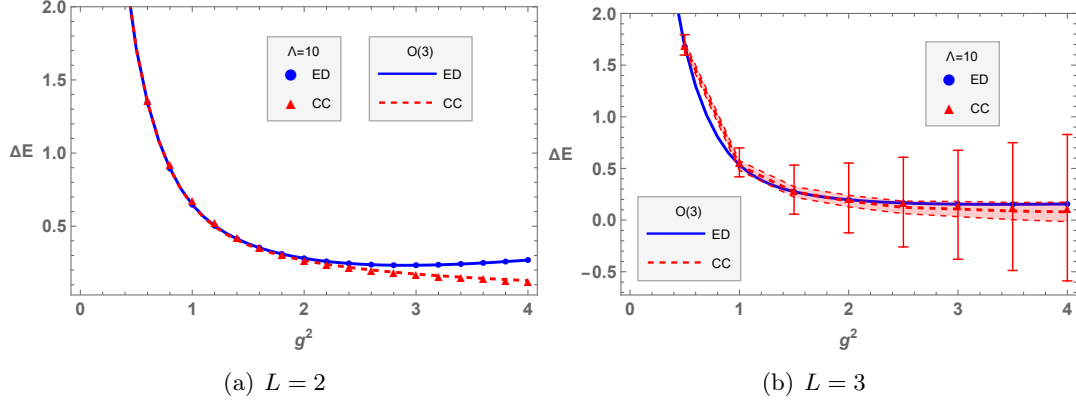


Figure 12. Mass gap ΔE for $L = 2, 3$ vs g^2 , computed with ED and the CC method, for $\Lambda = 10$. ED is taken at $l_{\max} = 3$.

be treated similarly), we define

$$|\Omega_x(\Lambda)\rangle \propto \phi_3(x) |\Omega(\Lambda)\rangle, \quad (3.12)$$

and for the first excited state, we apply the following CC Ansatz

$$|\text{CC}_1(\Lambda)\rangle \propto e^{-\frac{\alpha}{L} \sum_x (\phi(x) - \phi(x+1))^2} \sum_x |\Omega_x(\Lambda)\rangle. \quad (3.13)$$

This Ansatz reduces to the one for the $O(3)$ model, see Eq. (2.17), in the limit $\Lambda \rightarrow \infty$. The state $|\Omega_x(\Lambda)\rangle$, given by (3.12), is the weak-coupling eigenstate with site x in the state $|l(x) = 1, m(x) = 0; \Lambda\rangle$, and all others in the $|l(x') = 0, m(x') = 0; \Lambda\rangle$ state ($x' \neq x$). The degeneracy persists even at finite coupling, and so it should not matter which value of m we choose at x . The first excited state energies obtained from the CC method are shown in Fig. 14. As with the ground state, we find very good agreement with ED for large values of Λ . [GS: Why are we only comparing CC with ED at infinite Λ ? In particular, we should be comparing with Figure ?? . Maybe combine the two figures?]

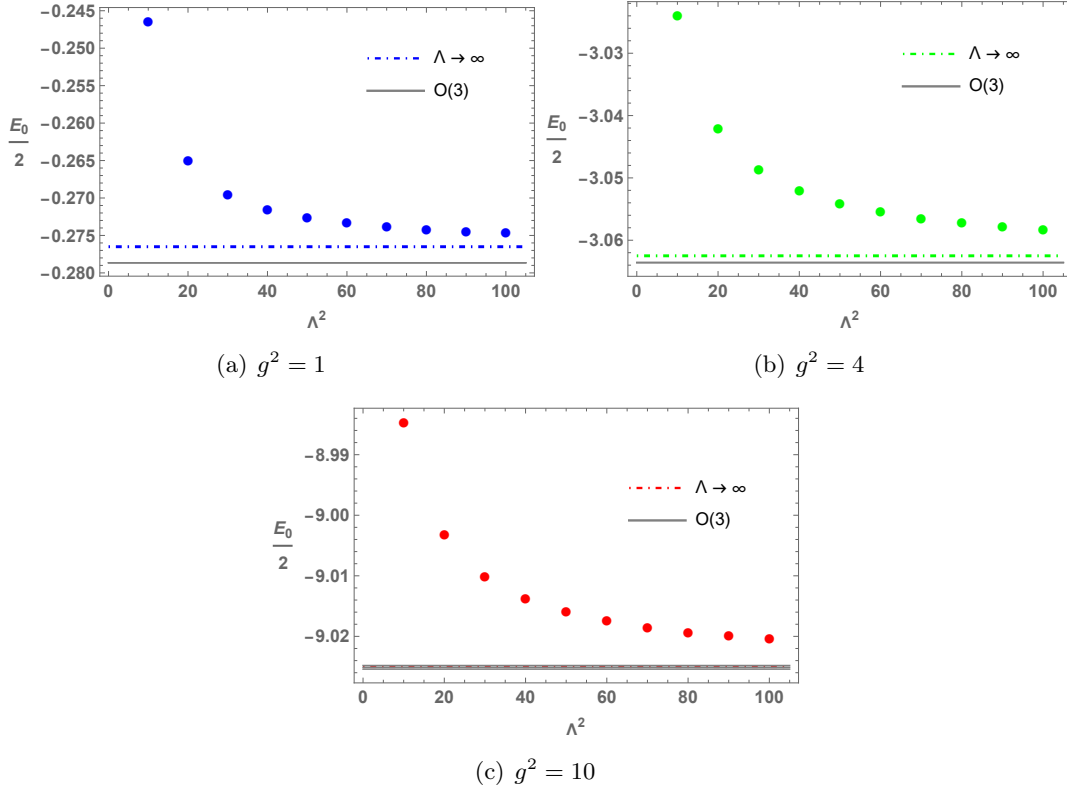


Figure 13. Minimized coupled cluster energies for the ground state, for different values of Λ in the state $|l=0, m=0; \Lambda\rangle$, and $L=2$. The shaded gray band is the $O(3)$ energy obtained from exact diagonalization, whose center is at $l_{\max}=10$ and the error given by its difference from $l_{\max}=9$. The $g^2=10$, $\Lambda \rightarrow \infty$ result is within the error region, indicating excellent agreement even for large g^2 .

4 Quantum simulation using continuous variables

In this section, we discuss the simulation of the $O(3)$ model using CV gates. We start with the construction of the CC Ansatz, which we then use for the quantum computation of energy levels. Next, we describe the relevant circuits for the time evolution within the CV approach and we present numerical results using the STRAWBERRY FIELDS quantum simulator. More detailed discussions about CV gates can be found in the Appendix A.

4.1 Coupled Cluster Ansatz

To engineer the CC Ansatz in (3.10), let us first concentrate on a single lattice site. By making use of three qumodes of quadratures (q_a, p_a) ($a=1, 2, 3$), collectively denoted as (\mathbf{q}, \mathbf{p}) , we initialize the system in the vacuum state

$$|0\rangle \equiv \bigotimes_{a=1}^3 |0\rangle_a = \frac{1}{\pi^{3/4}} \int d^3 \mathbf{q} e^{-\frac{1}{2} \mathbf{q}^2} |\mathbf{q}\rangle \quad (4.1)$$

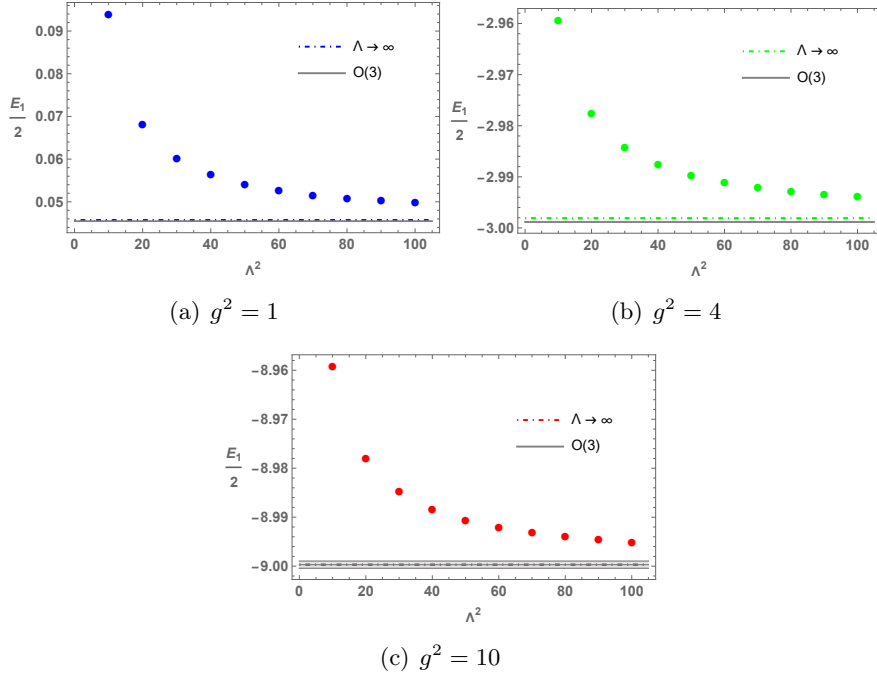


Figure 14. Minimized coupled cluster energies for the first excited state, for different values of Λ in the state $|l=0, m=0; \Lambda\rangle$. The shaded gray region is the $O(3)$ energy obtained from exact diagonalization, whose center is at $l_{\max} = 10$ and the error given by its difference from $l_{\max} = 9$. The $g^2 = 10$ $\Lambda \rightarrow \infty$ result is within the error region, indicating excellent agreement even for large g^2 .

We attach an ancilla qumode of quadratures (q_b, p_b) , also initialized in the vacuum state

$$|0\rangle_b = \frac{1}{\pi^{1/4}} \int dq_b e^{-\frac{1}{2}q_b^2} |q_b\rangle_b. \quad (4.2)$$

We apply the product of two-mode entangling non-Gaussian unitaries

$$U_{ab} = e^{-i \frac{\Lambda}{\sqrt{2}g} q_a^2 p_b}, \quad (4.3)$$

followed by the application of a translation operator on the ancilla qumode

$$U_b = e^{ig\sqrt{\frac{\Lambda^2}{2}+1} p_b}. \quad (4.4)$$

These operators shift the quadrature q_b of the ancilla qumode. Altogether, we thus obtain

$$U_b \prod_{a=1}^3 U_{ab} |0\rangle |0\rangle_b = \frac{1}{\pi} \int d^3 \mathbf{q} dq_b e^{-\frac{1}{2}\mathbf{q}^2} e^{-\frac{1}{2}\left[q_b - \frac{\Lambda}{\sqrt{2}g} \left(\mathbf{q}^2 - \left(1 + \frac{2}{\Lambda^2}\right)g^2\right)\right]^2} |\mathbf{q}\rangle |q_b\rangle_b. \quad (4.5)$$

Next, we measure the ancilla qumode projecting it onto the state $|0\rangle_b$. The resulting state, which we denote by $|\omega(\Lambda)\rangle$, now only involves the three main qumodes. It is given by

$$|\omega(\Lambda)\rangle \propto {}_b\langle 0| U_b \prod_{a=1}^3 U_{ab} |0\rangle |0\rangle_b \propto \int d^3 \mathbf{q} e^{-\frac{\Lambda^2}{8g^2}(\mathbf{q}^2 - g^2)^2} |\mathbf{q}\rangle. \quad (4.6)$$

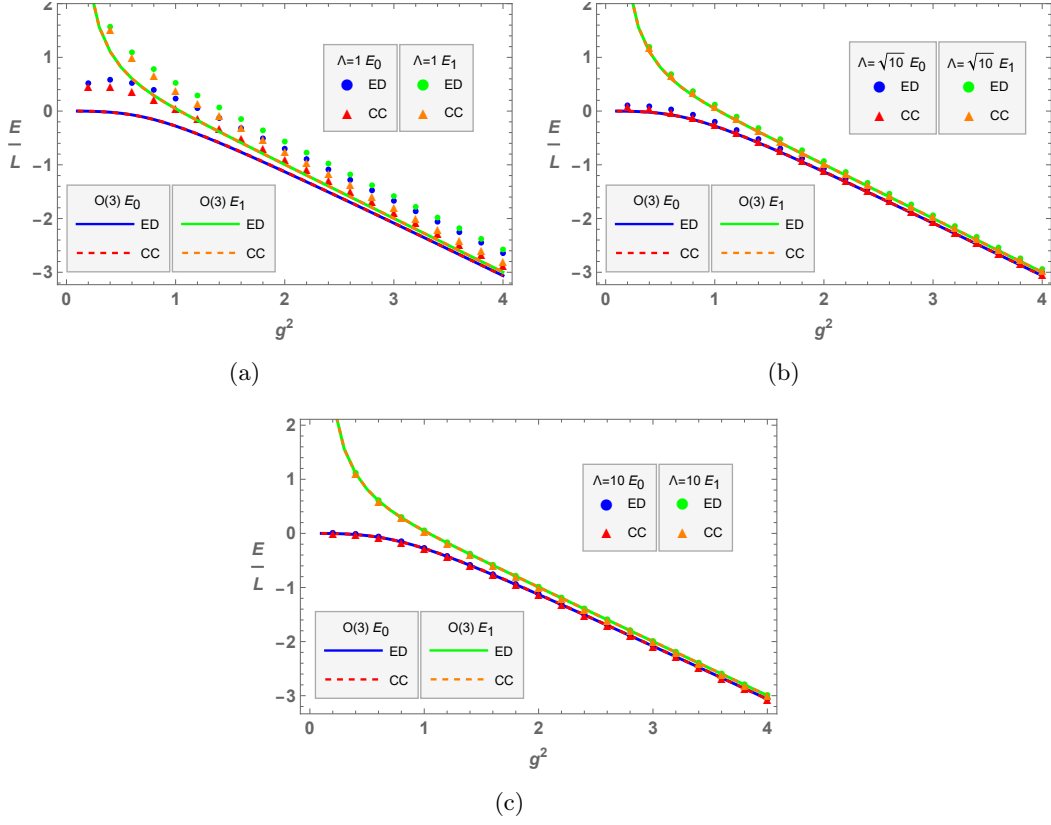


Figure 15. $L = 2$ ground and first excited state energies *vs* g^2 for different values of Λ , computed using exact diagonalization (ED) as well as via the coupled cluster (CC) method. ED uses a matrix truncation of $l_{\max} = 5$, while CC employs numerical integration.

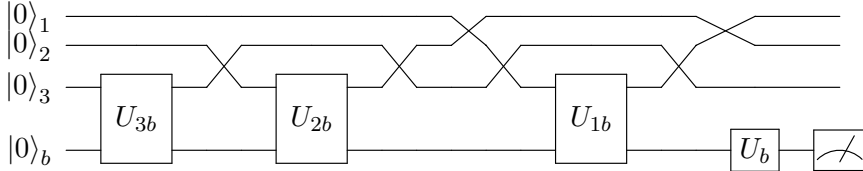


Figure 16. CV quantum circuit for the generation of the state $|\omega(\Lambda)\rangle = |l = 0, m = 0, \Lambda\rangle$ relevant for the construction of the coupled cluster ansatz, see (4.6).

Evidently, we constructed the state $|\omega(\Lambda)\rangle = |l = 0, m = 0, \Lambda\rangle$. The associated circuit in terms of CV gates is shown in Fig. 16. The non-Gaussian unitaries U_{ab} in (4.3) can be expressed in terms of cubic phase gates acting on the ancilla qumode. Using the relation

$$6q_a^2 p_b = (q_a + p_b)^3 - (q_a - p_b)^3 - 2p_b^3, \quad (4.7)$$

we obtain the following decomposition of U_{ab} :

$$U_{ab} = CZ_{ab}^\dagger \cdot F_b^\dagger \cdot V_b^\dagger \cdot F_b \cdot CZ_{ab}^2 \cdot F_b^\dagger \cdot V_b^\dagger \cdot F_b \cdot CZ_{ab}^\dagger \cdot F_b^\dagger \cdot V_b^2 \cdot F_b. \quad (4.8)$$

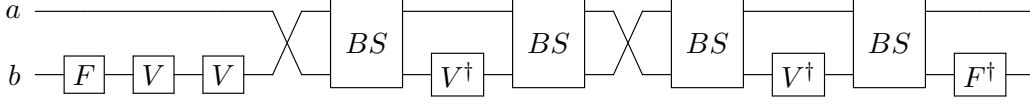


Figure 17. CV quantum circuit implementing the non-Gaussian unitary operator U_{ab} given in (4.3).

Here $F_b = e^{i\frac{\pi}{4}(p_b^2 + q_b^2)}$ is the Fourier transform operator, $CZ_{ab} = e^{iq_a p_b}$ is the controlled phase gate, (FR: CZ or CX? see appendix) and we introduced the cubic gate

$$V_b = e^{i\frac{\Lambda}{6\sqrt{2}g}q_b^3} . \quad (4.9)$$

We find that we can obtain better numerical accuracy when using the quantum simulator STRAWBERRY FIELDS¹ if we rewrite (4.8) in terms of beam splitters BS rather than CZ gates

$$U_{ab} = F_b^\dagger \cdot BS_{ba} \cdot V_b^\dagger \cdot BS_{ba} \cdot BS_{ab} \cdot V_b^\dagger \cdot BS_{ab} \cdot V_b^2 \cdot F_b , \quad (4.10)$$

Here BS_{ab} implements a 50:50 beam splitter (\leftarrow Write out explicitly, $\theta..?$) and BS_{ba} is the same beam splitter with ports switched. The quantum circuit for this unitary is shown in Figure 17.

Next, we consider two lattice sites each occupied by qumode triplets of quadratures (q_a, p_a) and (q'_a, p'_a) , respectively with $a = 1, 2, 3$. (\leftarrow should it be indices a, a' , see below?) As before, we collectively denote them by (\mathbf{q}, \mathbf{p}) and $(\mathbf{q}', \mathbf{p}')$. Analogous to the procedure discussed above, we start by engineering the state

$$|\omega(\Lambda)\rangle_a \otimes |\omega(\Lambda)\rangle_{a'} = |l = 0, m = 0; \Lambda\rangle \otimes |l' = 0, m' = 0; \Lambda\rangle , \quad (4.11)$$

which is given in terms of a direct tensor product of the states constructed for each lattice site, see (4.6). We proceed by attaching a triplet of ancilla qumodes of quadratures $(\mathbf{q}_c, \mathbf{p}_c)$ initialized in the vacuum state, and apply the Gaussian unitary

$$V_{ac} = e^{-i\sqrt{\frac{\alpha}{2L}}\mathbf{q}\cdot\mathbf{p}_c} \quad (4.12)$$

followed by the analogous unitary $V_{a'c}^\dagger$. These two operators shift the quadratures of the ancilla qumodes. We obtain the state

$$\begin{aligned} V_{a'c}^\dagger V_{ac} |\omega(\Lambda)\rangle_a \otimes |\omega(\Lambda)\rangle_{a'} &= \int d^3\mathbf{q} d^3\mathbf{q}' d^3\mathbf{q}_c e^{-\frac{1}{2}(\mathbf{q}^2 + \mathbf{q}'^2 + \mathbf{q}_c^2)} e^{-\frac{\Lambda^2}{8g^2}(\mathbf{q}^2 - g^2)^2} e^{-\frac{\Lambda^2}{8g^2}(\mathbf{q}'^2 - g^2)^2} \\ &\quad \times |\mathbf{q}\rangle |\mathbf{q}'\rangle |\mathbf{q}_c - \sqrt{\frac{\alpha}{2L}}(\mathbf{q} - \mathbf{q}')\rangle . \end{aligned} \quad (4.13)$$

¹However, in both cases, it is important that the gate set we use in STRAWBERRY FIELDS consists of entangling gates where “qumode 1” is the ancilla. Evidently, a gate set consisting of entangling gates with reverse ordering causes significant numerical problems.

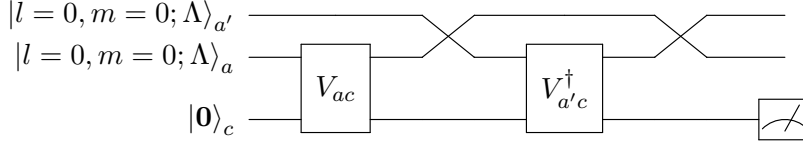


Figure 18. CV quantum circuit for constructing the CC state for two lattice sites in (4.14). Each line represents three qumodes. (Measurement vs projection onto $|0\rangle_c$ in circuit diagram, see Fig. below?)

After measuring the ancilla qumodes and projecting them onto the vacuum state $|0\rangle_c$, we obtain the state

$$e^{-\frac{\alpha}{L}(\mathbf{q}-\mathbf{q}')^2} |\omega(\Lambda)\rangle_a \otimes |\omega(\Lambda)\rangle_{a'} . \quad (4.14)$$

After identifying $\phi(x) = \mathbf{q}$, $\phi(x+1) = \mathbf{q}'$, we have thus engineered the desired state $|\text{CC}(\Lambda)\rangle$ for two lattice sites, see (3.10). The circuit to construct this state is shown in Fig. 18. This can be generalized to an arbitrary number of lattice sites by repeating the above procedure for each pair of adjacent sites $(x, x+1)$ of the 1-dimensional lattice.

Next, we are going to consider the construction of the first excited state, see (3.13) above. The construction of this state is a direct extension of the procedure for the ground state given in (3.10), which we have already engineered. After obtaining the state $|\Omega(\Lambda)\rangle$, (\leftarrow clarify relation between $|\omega(\Lambda)\rangle$ and $|\Omega(\Lambda)\rangle$..?) we add an ancilla of quadratures (q_c, p_c) prepared in the vacuum state $|0\rangle_c$. We then apply the following string of Gaussian unitaries (CX gates)

$$\prod_x e^{-i\gamma\phi_3(x)\otimes p_c}, \quad \gamma \ll 1, \quad (4.15)$$

and measure the added ancilla in the photon number basis projecting it onto the single-photon state. It is important that γ is chosen to be sufficiently small to increase the probability of success of the projective measurement and avoid introducing an unwanted dependence of the outcome on ϕ_3 . We obtain the following uniform superposition of states

$${}_c\langle 1| \prod_x e^{-i\gamma\phi_3(x)\otimes p_c} |\Omega(\Lambda)\rangle |0\rangle_c \propto \sum_x \phi_3(x) |\Omega(\Lambda)\rangle, \quad (4.16)$$

on which the CC Ansatz for the first-excited state (3.13) is based. The quantum circuit for $L = 2$ lattice sites is shown in Fig. 19. After obtaining the state in (4.16), we still need to apply the circuit show in Fig. 18 to realize the full CC Ansatz analogous to the ground state described above.

4.2 Quantum computation of energy levels

After constructing the CC Ansatz in the previous section, we are now going to describe the procedure to obtain the ground state energy of the Hamiltonian given in (3.2) using quantum resources. In order to compute the expectation value $\langle H \rangle$, we first consider the

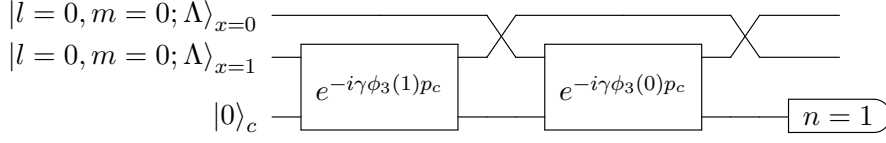


Figure 19. CV quantum circuit relevant for constructing the CC ansatz for the first excited state, see (3.13), with $L = 2$ lattice sites.

interaction term in (3.2), which is given by $\frac{1}{2} \sum_x (\phi(x) - \phi(x+1))^2$. After engineering the CC Ansatz, see (3.10), we create the state

$$|\Psi(\Gamma)\rangle \equiv \prod_x \prod_a P_{x,a}(\Gamma) \cdot BS_{x,x+1}^a |\text{CC}\rangle, \quad (4.17)$$

by acting on the CC Ansatz first with a series of 50:50 beam splitters with neighboring lattice sites as input ports and then by applying quadratic phase gates $P_{x,a}(\Gamma) = e^{i\Gamma\phi_a^2(x)/2}$, where Γ is a real parameter. Note that the quadratic phase gate can be decomposed in terms of a single rotation and single-mode squeezer gate. We then compute

$$\frac{1}{\Gamma^2} \sum_x \sum_a [\langle\Psi(\Gamma)| N_{x,a} |\Psi(\Gamma)\rangle + \langle\Psi(-\Gamma)| N_{x,a} |\Psi(-\Gamma)\rangle - 2\langle\Psi(0)| N_{x,a} |\Psi(0)\rangle], \quad (4.18)$$

where $N_{x,a}$ is the number operator for the qumode labeled by x, a , which can be written as $N_{x,a} = \frac{1}{2}(\pi_a^2(x) + \phi_a^2(x))$ with $a = 1, 2, 3$. To see why this gives us the expectation value of the interaction term of the Hamiltonian in (3.2), note that for a single qumode of quadratures (q, p) , we have

$$P^\dagger(\Gamma)NP(\Gamma) = \frac{1}{2} \left(q^2 + (p + \Gamma q)^2 \right), \quad (4.19)$$

where $N = \frac{1}{2}(p^2 + q^2)$ and $P(\Gamma)$ is the quadratic phase gate as introduced above. We deduce the following parameter shift rule

$$\frac{1}{\Gamma^2} \left[P^\dagger(\Gamma)NP(\Gamma) + P^\dagger(-\Gamma)NP(-\Gamma) - 2N \right] = q^2. \quad (4.20)$$

This yields the expression involving expectation values given in (4.18) by taking $q = \phi_a(x)$, and noting that applying the 50:50 beam splitters results in $\phi_a(x) \rightarrow \phi_a(x) - \phi_a(x+1)$. Therefore, we obtain the desired expression for the interaction term in the Hamiltonian in (3.2). A quantum circuit for the above calculation is shown in Fig. 20 for qumodes $\phi_a(x)$ and $\phi_a(x+1)$.

For practical purposes, when computing expectation values, it is advantageous to add an ancilla qumode of quadratures (q_c, p_c) prepared in the vacuum state and to use a CX gate instead of a P gate. That is, we make the replacement $e^{i\Gamma\phi_a^2(x)/2} \rightarrow e^{-i\Gamma p_c \otimes \phi_a(x)}$. This reduces numerical errors at small values of Γ , which is necessary to keep truncation errors

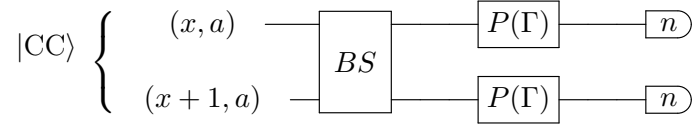


Figure 20. Quantum circuit for the calculation of the expectation value of the interaction term in the Hamiltonian (3.2) for qumodes $\phi_a(x)$ and $\phi_a(x+1)$.

and additional squeezing minimal. Instead of a parameter shift rule, we need to choose only one value of Γ and compute

$$\frac{2}{\Gamma^2} \langle \Psi(\Gamma) | N | \Psi(\Gamma) \rangle. \quad (4.21)$$

This gives the desired result due to the relation

$$CX(-\Gamma) \cdot N_c \cdot CX(\Gamma) = N_c + \Gamma q_c \phi_a(x) + \frac{\Gamma^2}{2} \phi_a^2(x), \quad (4.22)$$

where the expectation values of N_c and q_c vanish for the vacuum state, which the ancilla is prepared in. The only remaining term is the one we need, thereby preventing errors derived from unphysical terms. However, with only one ancilla this method requires us to compute $\langle (\Delta \phi_a(x))^2 \rangle$ for each value of x and a .

Next, we are going to consider the kinetic energy term in the Hamiltonian (3.2), which is given by

$$\frac{1}{2g^2} \sum_x L^2(x) = \frac{1}{2g^2} \sum_x (\phi(x) \times \pi(x))^2. \quad (4.23)$$

To obtain its expectation value, fix x and $a = 3$ and consider $\langle L_3^2(x) \rangle$ (the contributions of the other components are treated similarly). We compute the expectation value of the square of the number operator for the $a = 1, 2$ qumodes at lattice site x as:

$$\Delta N_{12}(x) \equiv (N_{x,2} - N_{x,1})^2 \quad (4.24)$$

with respect to the state

$$|\Psi\rangle \equiv BS_{12,x} \cdot F_{x,1} |\text{CC}\rangle \quad (4.25)$$

where F is the Fourier transform operator ($F = e^{i\frac{\pi}{4}(p^2+q^2)}$) and BS is a 50:50 beam splitter. After some algebra, we obtain

$$L_3^2(x) = F_{x,1}^\dagger \cdot BS_{12,x} \cdot \Delta N_{12}(x) \cdot BS_{12,x} \cdot F_{x,1} \quad (4.26)$$

hence

$$\langle \text{CC} | L_3^2(x) | \text{CC} \rangle = \langle \Psi | \Delta N_{12}(x) | \Psi \rangle \quad (4.27)$$

The expectation values of $L_{1,2}^2(x)$ are obtained by cyclic permutation of the indices.

However, with matrices anything beyond $L = 4, l_{\max} = 2$ where H is of size $9^4 \times 9^4$ presents a computational challenge. Therefore, we will use the numerical integration method to obtain energy estimates for a larger number of sites. In obtaining direct integration results

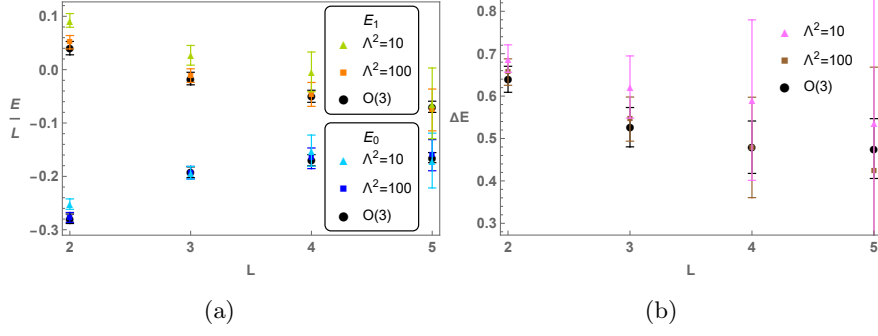


Figure 21. (a) Ground and first excited state coupled cluster energies for the $O(3)$ model for up to $L = 5$ sites, for $g^2 = 1$. We used quasi-Monte Carlo integration with 500,000 sample points. (b) Mass gaps $\Delta E = E_1 - E_0$.

for $L = 2$, the angular integrals could be performed analytically, and then we did numerical integration over the $r(x)$ to obtain CC energies for different values of R . For $L \geq 3$, we instead perform Monte Carlo integration over all variables.

The $g^2 = 1$ energies are displayed in Fig. 21. The mass gap appears to converge near $\Delta \simeq 0.48$ as $L \rightarrow \infty$. We see the accumulation of numerical error as the number of sites is increased, especially for smaller Λ . Results for $g^2 = 4$ are shown in Figure 22, with 10 times as many sample points. The gap at large L is very small, as expected, however, the numerical error is far more severe than the $g^2 = 1$ case, making it difficult to determine the gap at more than four sites.

STRAWBERRY FIELDS simulation results are depicted in Figure 23 for $g^2 = 1$ and $g^2 = 4$, for the ground state coupled cluster energies. Here we employed an ancilla and CX gates instead of P gates to compute the coupling term, see Eqs. (4.21) and (4.22). Error bars were obtained by computing the energy along each Cartesian direction. Since the CC ground state is invariant under global rotations, each result (multiplied by 3) should be valid, so that any variation derives from truncation error. Noticing the very significant truncation error at $\Lambda^2 = 10$ for Hilbert space dimensions of up to 14^7 (the extra qumode the ancilla), we see that it requires an immense amount of computational resources to be able to simulate a coupled cluster state with a sufficiently large value of Λ to estimate the $O(3)$ energies. The results at higher n_{\max} seem to be improved somewhat if we compute $\langle L^2 \rangle$ using Eq. (4.27) but by breaking up the expectation value as

$$\langle CC | L_3^2(x) | CC \rangle = 2 (\langle \Psi | N_1^2(x) | \Psi \rangle + \langle \Psi | N_2^2(x) | \Psi \rangle) - \langle CC | (N_1 + N_2)^2 | CC \rangle \quad (4.28)$$

where the last term is an expectation in the state $|CC\rangle$ rather than $|\Psi\rangle$, see Figure 24. [ST: Figure 23 on the other hand uses $|\Psi\rangle$ for all terms:

$$\langle CC | L_3^2(x) | CC \rangle = (\langle \Psi | N_1^2(x) | \Psi \rangle + \langle \Psi | N_2^2(x) | \Psi \rangle) - 2 \langle \Psi | N_1 N_2 | \Psi \rangle \quad (4.29)$$

] In any case, we note that the truncation error is in the number basis, unlike our ED results which were truncated in the spherical harmonic basis.

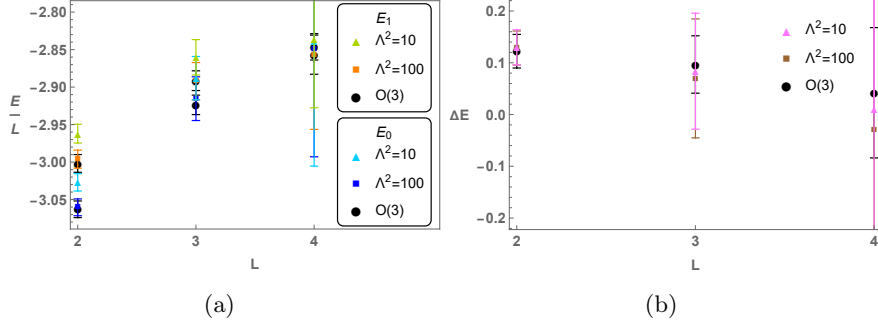


Figure 22. (a) Ground and first excited state coupled cluster energies for the $O(3)$ model for up to $L = 4$ sites, for $g^2 = 4$. We used quasi Monte Carlo integration with 5,000,000 sample points. Numerical error increases significantly beyond three sites. (b) Mass gaps $\Delta E = E_1 - E_0$.

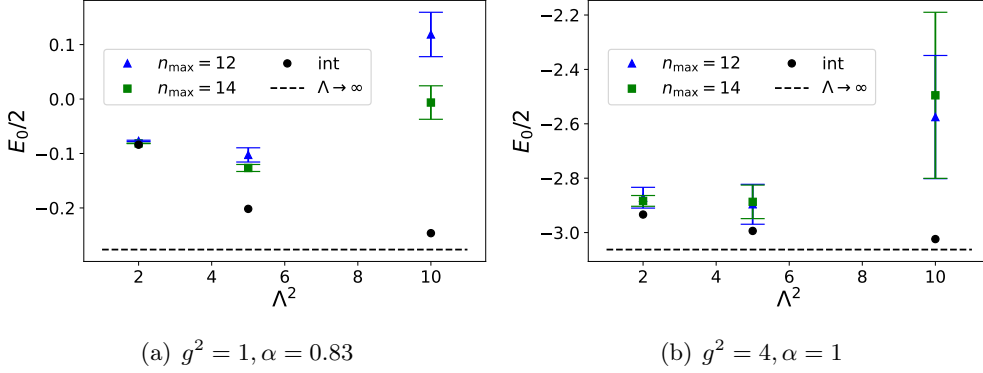


Figure 23. STRAWBERRY FIELDS simulation results for the calculation of ground state coupled cluster energies near the minimizing value of α for (a) $g^2 = 1$ and (b) $g^2 = 4$ and $L = 2$. The black points were obtained with numerical integration over the radial coordinates, and the dashed line obtained using Eq. (2.15).

4.3 Time evolution circuits and quantum simulator results

In this section, we perform the time evolution for the Hamiltonian given by (3.2).

To promote the interaction term in the Hamiltonian (3.2) to a time-evolution operator, we apply the string of unitaries $U_I \equiv \prod_x \prod_a U_a(x)$, where $U_a(x)$ is obtained by applying 50:50 beam splitters and a quadratic phase gate:

$$U_a(x) \equiv e^{-i\frac{\Delta t}{2}(\phi_a(x) - \phi_a(x+1))^2} = BS_{x,x+1}^a \cdot P_{x,a}\left(-\frac{\Delta t}{2}\right) \cdot BS_{x,x+1}^a \quad (4.30)$$

A quantum circuit implementing this Trotter step is shown in Figure 25 for qumodes $\phi_a(x)$ and $\phi_a(x+1)$.

The time evolution of the kinetic term can be implemented with the aid of non-Gaussian Kerr gates, $K(s) = e^{isN^2}$, and Cross-Kerr gates, $CK(s) = e^{isN_1N_2}$. For a given lattice site x , each Trotter step will contain the string of unitaries

$$U_{31}(x) \cdot U_{23}(x) \cdot U_{12}(x) \quad (4.31)$$

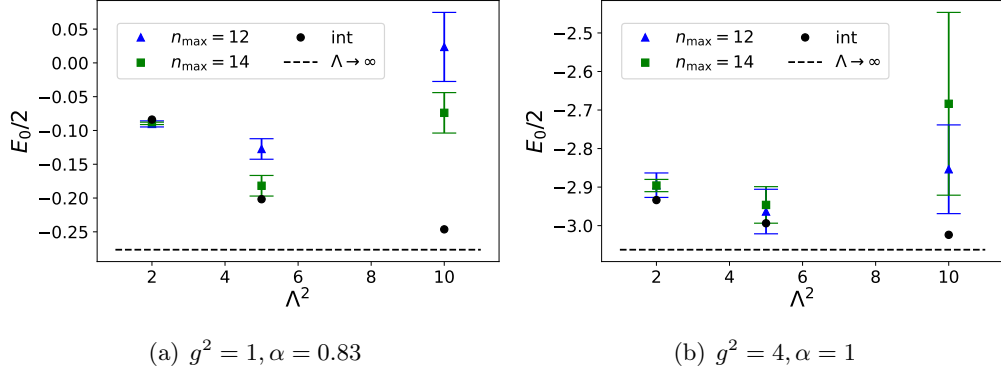


Figure 24. STRAWBERRY FIELDS simulation results for the calculation of ground state coupled cluster energies near the minimizing value of α for (a) $g^2 = 1$ and (b) $g^2 = 4$ and $L = 2$. Here we use (4.28) to compute the kinetic energy. The black points were obtained with numerical integration over the radial coordinates, and the dashed line obtained using Eq. (2.15).

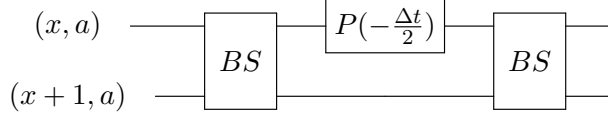


Figure 25. Quantum circuit for a Trotter step of the interaction term (Eq. (4.30)) in the Hamiltonian (3.2) for qumodes $\phi_a(x)$ and $\phi_a(x+1)$.

where, using Eq. (4.26),

$$U_{ab}(x) = F_{x,a}^\dagger \cdot BS_x^{ab} \cdot K_{x,a}(-\frac{\Delta t}{2g^2}) \cdot CK_x^{ab}(\frac{\Delta t}{g^2}) \cdot K_{x,b}(-\frac{\Delta t}{2g^2}) \cdot BS_x^{ab} \cdot F_{x,a} \quad (4.32)$$

A quantum circuit implementing the Trotter step for the kinetic energy (4.31) is shown in Figure 26 for the three qumodes at a given lattice site x .

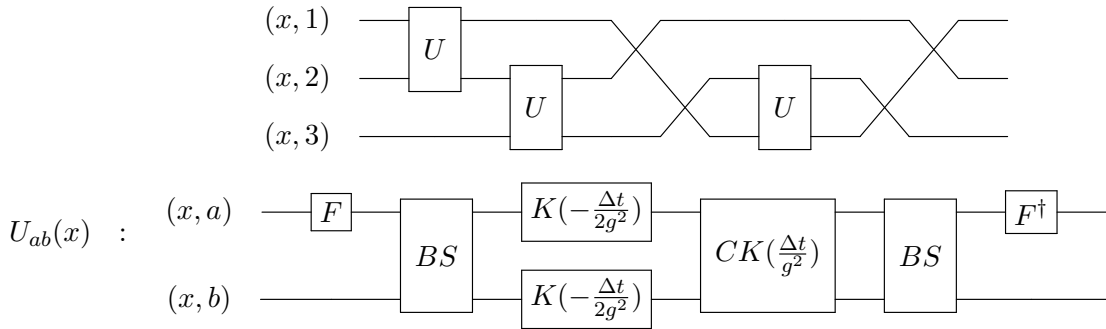


Figure 26. CIRC6 Quantum circuit for a Trotter step of the kinetic energy (Eq. (4.31)) in the Hamiltonian (3.2) for the three qumodes $\phi_a(x)$.

Having described the protocol for time evolution, we now quantify the errors accrued during the evolution. In particular, we show that for a long time of evolution, t , the error in the computed amplitudes is $\mathcal{O}\left(\frac{t^2}{\Lambda^2}\right)$, which tells us that given any time t , we can fix Λ so that we obtain the $O(3)$ result to the desired accuracy.

Consider the state $|l, m; \Lambda\rangle$ given by Eq. (3.4). Its wavefunction factorizes into radial and angular parts,

$$\langle r, \mathbf{n} | l, m; \Lambda \rangle = \psi_\Lambda(r) Y_{lm}(\mathbf{n}) , \quad \psi_\Lambda(r) = \frac{1}{\sqrt{\mathcal{N}}} e^{-\Lambda^2(r^2 - g^2)^2 / 8g^2} \quad (4.33)$$

where the normalization constant is given by (3.5) for large cutoff Λ . The radial wavefunction is centered at $r = g$ with a spread $\Delta r \sim \mathcal{O}(1/\Lambda)$. The matrix elements of the evolution operator in the basis (3.4) can be written as

$$\langle \mathbf{l}, \mathbf{m}; \Lambda | e^{-itH} | \mathbf{l}', \mathbf{m}'; \Lambda \rangle = \int \prod_x dr(x) r^2(x) |\psi_\Lambda(r(x))|^2 \langle \mathbf{l} \mathbf{m} | e^{-itH} | \mathbf{l}' \mathbf{m}' \rangle . \quad (4.34)$$

where $|\mathbf{l}, \mathbf{m}; \Lambda\rangle = \bigotimes_x |l(x), m(x); \Lambda\rangle$, and similarly for the other states. The Hamiltonian H is a function of the radial coordinates through its interaction term which is quadratic in the fields. Therefore, the radial spread in the exponent of the evolution operator is $t \cdot \mathcal{O}(r\Delta r) \sim \mathcal{O}(gt/\Lambda)$, where we used $r \sim g$ and $\Delta r \sim 1/\Lambda$. It follows that, given t , we should choose Λ so that $t \lesssim \Lambda/g$. To show this numerically, we computed the probability corresponding to the transition amplitudes (4.34) for several values of Λ and $g^2 = 1$. Results are shown in Figs. 27 and 28. **Discuss results.** In Fig. 27, we computed this probability for $l = l' = m = m' = 0$ and for three different times, for $L = 2$ sites. As in (4.34), this calculation was performed by expressing the time evolution operator as a matrix in the spherical harmonic basis, and as a function of the continuous parameter r . Monte Carlo integration was then performed over the r coordinate to complete the computation of the amplitude. We find that greater values of Λ are required for large times t as well as for values of t for which the returning probability is also large.

In Fig. 28, we analyzed the time evolution using a STRAWBERRY FIELDS simulation. Instead of computing an amplitude in the basis $|\mathbf{l}, \mathbf{m}; \Lambda\rangle$, we constructed and evolved the state $|\mathbf{0}, \mathbf{0}; \Lambda\rangle$ but computed the amplitude with the photon number vacuum state

$$\langle \mathbf{r} | \mathbf{0} \rangle \propto e^{-r^2/2} | \mathbf{l} = 0, \mathbf{m} = 0 \rangle \quad (4.35)$$

Even with just two Trotter steps and a small truncation in the photon number basis, the Figure displays good agreement with results obtained using matrices and Monte Carlo integration, the latter of which contains no Trotter error. **It is interesting that at larger times we get better agreement with $n_{\max} = 8, 10$ than with $n_{\max} = 12$.**

5 Conclusion

We studied the $O(3)$ sigma model in 1+1 dimensions using continuous variables which is an alternate approach to quantum computing. To achieve this, we considered a collection of scalar fields with three physical qumodes at each site. In the limit of sufficiently large

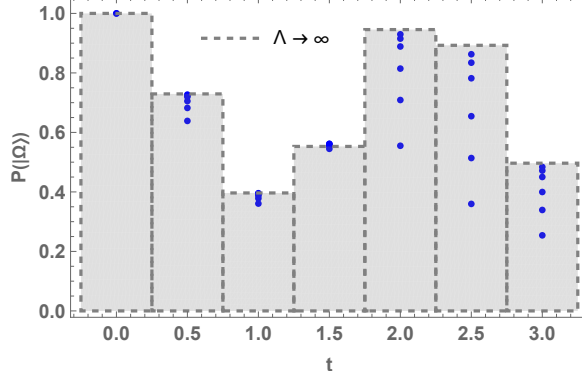


Figure 27. The probability of obtaining the original state $|\Omega(\Lambda)\rangle$ for several times t and for $L = 2, l_{\max} = 3, g^2 = 1$. The blue points correspond to $\Lambda^2 = 10, 20, 40, 100, 200, 400$, while the histogram values correspond to the $O(3)$ limit.

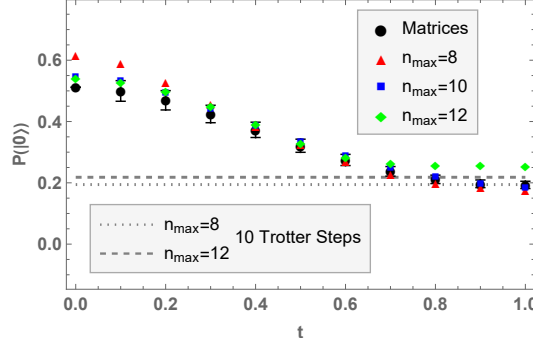


Figure 28. Probability of obtaining the vacuum state $|0\rangle$, after evolving the state $|\Omega(\Lambda)\rangle$ for a time t , for $L = 2, g^2 = 1, \Lambda^2 = 10$. The black points are obtained in the same way as in Figure 27 (matrices in spherical harmonic basis at truncation $l_{\max} = 3$, Monte Carlo integration over radial direction). The points without error bars indicate results obtained from STRAWBERRY FIELDS with 2 Trotter steps for different Fock space cutoffs n_{\max} . Also shown is the result for $n_{\max} = 8$ and $n_{\max} = 12$ with 10 Trotter steps.

squeezing, our results show that we agree with the lattice rotor Hamiltonian. In order to carry out the quantum simulation, we start by preparing the ground and excited states. To achieve this, we used the coupled cluster Ansatz and found that it accurately obtains the ground and excited state energies. Using this Ansatz, we outlined the procedure to compute the expectation value of the energy and perform time evolution using continuous variables. We estimated the resource requirements and the accuracy of time evolution to leading order in the radial cutoff Λ . To show that our outlined procedure works in practice, we prepared the ground state Ansatz and performed the time evolution for a few Trotter steps using the photonic simulator, STRAWBERRY FIELDS with appropriate truncation of the Fock space.

Acknowledgments

We would like to thank Jack Araz, Raul Briceno, Robert Edwards, and Kostas Orginos for helpful discussions. The research was supported by the U.S. Department of Energy, Office of Science, National Quantum Information Science Research Centers, Co-design Center for Quantum Advantage under contract number DE-SC0012704 and the U.S. Department of Energy, Office of Science, Office of Nuclear Physics under contract DE-AC05-06OR23177. GS and ST acknowledge support by DOE ASCR funding under the Quantum Computing Application Teams Program, the Army Research Office award W911NF-19-1-0397, NSF award DGE-2152168, and DOE award DE-SC0023687. RGJ and FR are supported by the U.S. Department of Energy, Office of Science, Contract No. DE-AC05-06OR23177, under which Jefferson Science Associates, LLC operates Jefferson Lab. FR is supported in part by the DOE, Office of Science, Office of Nuclear Physics, Early Career Program under contract No. DE-SC0024358. This research used resources of the Oak Ridge Leadership Computing Facility, which is a DOE Office of Science User Facility supported under Contract DE-AC05-00OR22725.

A Continuous Variable Gates

In this appendix we review some of the CV gates used in this paper. Additional details and gates can be found in [34].

A.1 Single qumode gates

To create a squeezed state on the sphere, we first apply a squeeze operation and then a displacement in position. Squeezing is implemented by

$$S(r) = e^{\frac{r}{2}(a^{\dagger 2} - a^2)}, \quad (\text{A.1})$$

where a and a^{\dagger} are bosonic creation and annihilation operators with $[a, a^{\dagger}] = 1$. The position and conjugate momentum are written as

$$q = \frac{1}{\sqrt{2}}(a^{\dagger} + a), \quad p = \frac{i}{\sqrt{2}}(a^{\dagger} - a) \quad (\text{A.2})$$

Recall that in this paper the components of the field $\phi_i(x)$, on each of L sites, give $3L$ independent position operators, each of which are accompanied by their conjugate momentum $\pi_i(x)$. It follows from (A.1) and (A.2) that

$$S^{\dagger}(r)qS(r) = e^{-r}q, \quad S^{\dagger}(r)pS(r) = e^r p \quad (\text{A.3})$$

Note that we have

$$r = \frac{1}{2} \ln R, \quad (\text{A.4})$$

where R is the squeezing parameter used in this paper. A displacement in position is possible using a displacement gate equipped with a real parameter

$$e^{-ipx} = D(x/\sqrt{2}) = e^{\frac{x}{\sqrt{2}}(a^{\dagger} - a)}, \quad x \in \mathbb{R} \quad (\text{A.5})$$

Its action is

$$q \rightarrow q + x, \quad p \rightarrow p \quad (\text{A.6})$$

This action gives us a way to compute the expectation value of q .

$$q = \frac{1}{2x} (e^{ipx} N e^{-ipx} - e^{-ipx} N e^{ipx}), \quad N = \frac{1}{2} (q^2 + p^2) \quad (\text{A.7})$$

Thus to compute $\langle \psi | q | \psi \rangle$, we compute the mean photon number in the two states

$$e^{-ipx} |\psi\rangle, \quad e^{ipx} |\psi\rangle \quad (\text{A.8})$$

and take the difference.

We also use a rotation gate

$$R(\theta) = e^{iN\theta}, \quad \theta \in \mathbb{R} \quad (\text{A.9})$$

to help in implementing the angular momentum operator \vec{L} . It rotates the position and momentum

$$\begin{pmatrix} q \\ p \end{pmatrix} \rightarrow \begin{pmatrix} \cos \theta & -\sin \theta \\ \sin \theta & \cos \theta \end{pmatrix} \begin{pmatrix} q \\ p \end{pmatrix} \quad (\text{A.10})$$

A particularly useful single-qumode gate is the quadratic phase gate,

$$P(s) = e^{isq^2/2}, \quad (\text{A.11})$$

which has the transformation properties

$$P^\dagger(s) q P(s) = q, \quad P^\dagger(s) p P(s) = p + sq \quad (\text{A.12})$$

From this we find

$$P^\dagger(s) N P(s) = P^\dagger(s) \frac{1}{2} (q^2 + p^2) P(s) = \frac{1}{2} [q^2 + (p + sq)^2] \quad (\text{A.13})$$

Thus

$$q^2 = \frac{1}{2s^2} (P^\dagger(s) N P(s) + P^\dagger(-s) N P(-s) - 2P^\dagger(0) N P(0)) \quad (\text{A.14})$$

This means that we can compute the expectation value $\langle \psi | q^2 | \psi \rangle$ by instead computing

$$\langle \psi | P^\dagger(s) N P(s) | \psi \rangle, \quad (\text{A.15})$$

for three values of s . These are found simply by measuring the mean photon number in the state $P(s) |\psi\rangle$. Note that it is possible to express the P gate in terms of the more elementary rotation and single-mode squeeze gates [34].

A.2 Two qumode gates

The fundamental two qumode gate that is typically considered is the beamsplitter gate

$$\text{BS}_{i,j}(\theta) = e^{\theta(a_i a_j^\dagger - a_i^\dagger a_j)}, \quad \theta \in \mathbb{R} \quad (\text{A.16})$$

We use it in conjunction with R in dealing with \vec{L} . Its action is given by

$$\begin{pmatrix} q_i/p_i \\ q_j/p_j \end{pmatrix} \rightarrow \begin{pmatrix} \cos \theta & -\sin \theta \\ \sin \theta & \cos \theta \end{pmatrix} \begin{pmatrix} q_i/p_i \\ q_j/p_j \end{pmatrix} \quad (\text{A.17})$$

We note that in our qumode formulation, the beamsplitter corresponds to an $O(3)$ rotation in the $x_i - x_j$ plane,

$$\text{BS}_{i,j}(\theta) = e^{-i\theta \epsilon_{ijk} L_k} \quad (\text{A.18})$$

Another important gate is the ‘CX’ gate,

$$\text{CX}_{i,j}(s) = e^{-isq_i p_j}, \quad (\text{A.19})$$

which can be decomposed in terms of beamsplitters and single-mode squeezers. Its action is

$$\begin{aligned} q_i &\rightarrow q_i, & p_i &\rightarrow p_i - sp_j \\ p_j &\rightarrow p_j, & q_j &\rightarrow q_j + sq_i \end{aligned} \quad (\text{A.20})$$

In this paper, we use this gate for two purposes. First, it allows us to obtain the difference in field ‘positions’,

$$\vec{\phi}(x) - \vec{\phi}(x+1) \quad (\text{A.21})$$

which appears in the coupling term of our Hamiltonian. Second, with the aid of an ancilla, it enables us to engineer certain exponential wavefunctions. Let q_i be a physical qumode and q_a an ancilla. Then

$$\text{CX}_{i,a}(s) |\psi\rangle_i \otimes |0\rangle_a = \int dq \langle q|\psi\rangle |q\rangle_i \otimes e^{-ip_a(sq)} |0\rangle_a = \int dq \langle q|\psi\rangle |q\rangle_i \otimes |sq\rangle_a \quad (\text{A.22})$$

The state $|sq\rangle_a$ is a coherent state, and so

$$\langle N=0|sq\rangle_a = e^{-s^2 q^2/2} \quad (\text{A.23})$$

Thus, measuring q_a to be in the $N=0$ state gives the (unnormalized) state

$$\int dq \langle q|\psi\rangle e^{-s^2 q^2/2} |q\rangle_i = e^{-s^2 q_i^2/2} |\psi\rangle_i \quad (\text{A.24})$$

This recipe allows us to apply the coupled cluster operator to the state $|\Omega(R)\rangle$. In this case we couple six physical modes to the ancilla at a time:

$$q_i p_a \rightarrow \left(\vec{\phi}(x) - \vec{\phi}(x+1) \right) p_a \quad (\text{A.25})$$

A similar procedure is used to construct $|\Omega(R)\rangle$ itself but requires more than just CX gates since the operation is non-Gaussian.

References

- [1] A. M. Polyakov, “Interaction of Goldstone Particles in Two-Dimensions. Applications to Ferromagnets and Massive Yang-Mills Fields,” [*Phys. Lett. B* **59** \(1975\) 79–81](#).
- [2] A. M. Polyakov and A. A. Belavin, “Metastable States of Two-Dimensional Isotropic Ferromagnets,” [*JETP Lett.* **22** \(1975\) 245–248](#).
- [3] B. Berg and M. Luscher, “Definition and Statistical Distributions of a Topological Number in the Lattice $O(3)$ Sigma Model,” [*Nucl. Phys. B* **190** \(1981\) 412–424](#).
- [4] F. Bruckmann, K. Jansen, and S. Kühn, “ $O(3)$ nonlinear sigma model in 1+1 dimensions with matrix product states,” [*Phys. Rev. D* **99** no. 7, \(2019\) 074501](#), [arXiv:1812.00944 \[hep-lat\]](#).
- [5] W. Tang, X. C. Xie, L. Wang, and H.-H. Tu, “Tensor network simulation of the $(1+1)$ -dimensional $O(3)$ nonlinear σ -model with $\theta=\pi$ term,” [*Phys. Rev. D* **104** no. 11, \(2021\) 114513](#), [arXiv:2109.11324 \[hep-lat\]](#).
- [6] J. F. Unmuth-Yockey, Y. Meurice, J. Osborn, and H. Zou, “Tensor renormalization group study of the 2d $O(3)$ model,” [*PoS LATTICE2014* \(2014\) 325](#), [arXiv:1411.4213 \[hep-lat\]](#).
- [7] H. Singh and S. Chandrasekharan, “Qubit regularization of the $O(3)$ sigma model,” [*Phys. Rev. D* **100** no. 5, \(2019\) 054505](#), [arXiv:1905.13204 \[hep-lat\]](#).
- [8] A. Alexandru, P. F. Bedaque, A. Carosso, and A. Sheng, “Universality of a truncated sigma-model,” [*Phys. Lett. B* **832** \(2022\) 137230](#), [arXiv:2109.07500 \[hep-lat\]](#).
- [9] J. Y. Araz, S. Schenk, and M. Spannowsky, “Towards a Quantum Simulation of Nonlinear Sigma Models with a Topological Term,” [arXiv:2210.03679 \[quant-ph\]](#).
- [10] S. Lloyd and S. L. Braunstein, “Quantum computation over continuous variables,” [*Phys. Rev. Lett.* **82** \(Feb, 1999\) 1784–1787](#).
<https://link.aps.org/doi/10.1103/PhysRevLett.82.1784>.
- [11] N. C. Menicucci, P. van Loock, M. Gu, C. Weedbrook, T. C. Ralph, and M. A. Nielsen, “Universal quantum computation with continuous-variable cluster states,” [*Phys. Rev. Lett.* **97** \(Sep, 2006\) 110501](#). <https://link.aps.org/doi/10.1103/PhysRevLett.97.110501>.
- [12] **NuQS** Collaboration, A. Alexandru, P. F. Bedaque, H. Lamm, and S. Lawrence, “ σ Models on Quantum Computers,” [*Phys. Rev. Lett.* **123** no. 9, \(2019\) 090501](#), [arXiv:1903.06577 \[hep-lat\]](#).
- [13] A. N. Ciavarella, S. Caspar, H. Singh, and M. J. Savage, “Preparation for quantum simulation of the $(1+1)$ -dimensional $O(3)$ nonlinear σ model using cold atoms,” [*Phys. Rev. A* **107** no. 4, \(2023\) 042404](#), [arXiv:2211.07684 \[quant-ph\]](#).
- [14] A. J. Buser, T. Bhattacharya, L. Cincio, and R. Gupta, “State preparation and measurement in a quantum simulation of the $O(3)$ sigma model,” [*Phys. Rev. D* **102** no. 11, \(2020\) 114514](#), [arXiv:2006.15746 \[quant-ph\]](#).
- [15] N. Killoran, J. Izaac, N. Quesada, V. Bergholm, M. Amy, and C. Weedbrook, “Strawberry Fields: A software platform for photonic quantum computing,” [*Quantum* **3** \(2019\) 129](#), [arXiv:1804.03159](#).
- [16] M. Eaton, A. Hossameldin, R. J. Birrittella, P. M. Alsing, C. C. Gerry, H. Dong, C. Cuevas,

- and O. Pfister, “Resolution of 100 photons and quantum generation of unbiased random numbers,” *Nature Photon.* **17** no. 1, (2023) 106–111, [arXiv:2205.01221 \[quant-ph\]](#).
- [17] L. S. Madsen, F. Laudenbach, M. F. Askarani, F. Rortais, T. Vincent, J. F. F. Bulmer, F. M. Miatto, L. Neuhaus, L. G. Helt, M. J. Collins, A. E. Lita, T. Gerrits, S. W. Nam, V. D. Vaidya, M. Menotti, I. Dhand, Z. Vernon, N. Quesada, and J. Lavoie, “Quantum computational advantage with a programmable photonic processor,” *Nature* **606** no. 7912, (2022) 75–81. <https://doi.org/10.1038/s41586-022-04725-x>.
 - [18] C. Taballione et al., “20-Mode Universal Quantum Photonic Processor,” *Quantum* **7** (2023) 1071, [arXiv:2203.01801 \[quant-ph\]](#).
 - [19] A. M. Polyakov, *Gauge Fields and Strings*, vol. 3. 1987.
 - [20] J. Kogut and L. Susskind, “Hamiltonian formulation of wilson’s lattice gauge theories,” *Phys. Rev. D* **11** (Jan, 1975) 395–408. <https://link.aps.org/doi/10.1103/PhysRevD.11.395>.
 - [21] C. J. Hamer, J. B. Kogut, and L. Susskind, “Strong Coupling Expansions and Phase Diagrams for the O(2), O(3) and O(4) Heisenberg Spin Systems in Two-dimensions,” *Phys. Rev. D* **19** (1979) 3091.
 - [22] T. T. Wu and C. N. Yang, “Some properties of monopole harmonics,” *Physical Review D* **16** no. 4, (Aug., 1977) 1018–1021. <https://doi.org/10.1103/physrevd.16.1018>.
 - [23] T. D. Crawford and H. F. Schaefer, “An introduction to coupled cluster theory for computational chemists,” Jan., 2000. <https://doi.org/10.1002/9780470125915.ch2>.
 - [24] W. Kutzelnigg, “Error analysis and improvements of coupled-cluster theory,” *Theoretica Chimica Acta* **80** no. 4-5, (1991) 349–386. <https://doi.org/10.1007/bf01117418>.
 - [25] N. E. Ligterink, N. R. Walet, and R. F. Bishop, “A Coupled cluster formulation of Hamiltonian lattice field theory: The nonlinear sigma model,” *Annals Phys.* **267** (1998) 97–133, [arXiv:hep-lat/9712021](#).
 - [26] N. Ligterink, N. Walet, and R. Bishop, “The ground state of the nonlinear sigma model o(4) in 3+1 dimensions,” *Nuclear Physics B - Proceedings Supplements* **63** no. 1-3, (Apr., 1998) 667–669. [https://doi.org/10.1016/s0920-5632\(97\)00866-9](https://doi.org/10.1016/s0920-5632(97)00866-9).
 - [27] I. G. Ryabinkin, T.-C. Yen, S. N. Genin, and A. F. Izmaylov, “Qubit coupled cluster method: A systematic approach to quantum chemistry on a quantum computer,” *Journal of Chemical Theory and Computation* **14** no. 12, (Nov., 2018) 6317–6326. <https://doi.org/10.1021/acs.jctc.8b00932>.
 - [28] E. F. Dumitrescu, A. J. McCaskey, G. Hagen, G. R. Jansen, T. D. Morris, T. Papenbrock, R. C. Pooser, D. J. Dean, and P. Lougovski, “Cloud Quantum Computing of an Atomic Nucleus,” *Phys. Rev. Lett.* **120** (2018) 210501, [arXiv:1801.03897 \[quant-ph\]](#).
 - [29] A. Duncan and R. Roskies, “Asymptotic scaling in hamiltonian calculations of the o(3) σ model,” *Phys. Rev. D* **32** (Dec, 1985) 3277–3281. <https://link.aps.org/doi/10.1103/PhysRevD.32.3277>.
 - [30] R. G. Jha, F. Ringer, G. Siopsis, and S. Thompson, “Toward quantum computations of the O(3) model using qumodes,” 8, 2023. [arXiv:2308.06946 \[hep-lat\]](#).
 - [31] Z. Davoudi, A. F. Shaw, and J. R. Stryker, “General quantum algorithms for Hamiltonian simulation with applications to a non-Abelian lattice gauge theory,” [arXiv:2212.14030 \[hep-lat\]](#).

- [32] K. Marshall, R. Pooser, G. Siopsis, and C. Weedbrook, “Quantum simulation of quantum field theory using continuous variables,” [*Phys. Rev. A* **92** no. 6, \(2015\) 063825](#), [arXiv:1503.08121 \[quant-ph\]](#).
- [33] S. Thompson and G. Siopsis, “Quantum Computation of Phase Transition in Interacting Scalar Quantum Field Theory,” [arXiv:2303.02425 \[quant-ph\]](#).
- [34] N. Killoran, J. Izaac, N. Quesada, V. Bergholm, M. Amy, and C. Weedbrook, “Strawberry fields: A software platform for photonic quantum computing,” [*Quantum* **3** \(Mar, 2019\) 129](#). <https://doi.org/10.22331/2Fq-2019-03-11-129>.